Glucose-6-Phosphate Dehydrogenase from the Human Pathogen *Trypanosoma cruzi* Evolved Unique Structural Features to Support Efficient Product Formation

Cecilia Ortíz [1], Horacio Botti [2,3], Alejandro Buschiazzo [2,4] and Marcelo A. Comini [1]

*1 - **Laboratory Redox Biology of Trypanosomes,** Institut Pasteur de Montevideo, Mataojo 2020, 11400 Montevideo, Uruguay*
*2 - **Laboratory of Molecular & Structural Microbiology,** Institut Pasteur de Montevideo, Mataojo 2020, 11400 Montevideo, Uruguay*
*3 - **Laboratory of Integrative Biophysics,** Departamento de Biofísica, Facultad de Medicina, Universidad de la República, Montevideo, Uruguay*
*4 - **Department of Microbiology,** Institut Pasteur, rue du Dr Roux, 75015 Paris, France*

***Correspondence to Alejandro Buschiazzo and Marcelo A. Comini:** A. Buschiazzo is to be contacted at: Laboratory of Molecular & Structural Microbiology, Institut Pasteur de Montevideo, Mataojo 2020, 11400 Montevideo, Uruguay.; M.A. Comini is to be contacted at: Laboratory Redox Biology of Trypanosomes, Institut Pasteur de Montevideo, 11400 Montevideo, Uruguay.*
alebus@pasteur.edu.uy; mcomini@pasteur.edu.uy
https://doi.org/10.1016/j.jmb.2019.03.023
Edited by Dan Tawfik

Abstract

Glucose-6-phosphate dehydrogenase (G6PDH) is the key enzyme supplying reducing power (NADPH) to the cells, by oxidation of glucose-6-phosphate (G6P), and in the process providing a precursor of ribose-5-phosphate. G6PDH is also a virulence factor of pathogenic trypanosomatid parasites. To uncover the biochemical and structural features that distinguish *Tc*G6PDH from its human homolog, we have solved and analyzed the crystal structures of the G6PDH from *Trypanosoma cruzi* (*Tc*G6PDH), alone and in complex with G6P. *Tc*G6PDH crystallized as a tetramer and enzymatic assays further indicated that the tetramer is the active form in the parasite, in contrast to human G6PDH, which displays higher activity as a dimer. This quaternary structure was shown to be particularly stable. The molecular reasons behind this disparity were unveiled by structural analyses: a *Tc*G6PDH-specific residue, R323, is located at the dimer–dimer interface, critically contributing with two salt bridges per subunit that are absent in the human enzyme. This explains why *Tc*G6PDH dimerization impaired enzyme activity. The parasite protein is also distinct in displaying a 37-amino-acid extension at the N-terminus, which comprises the non-conserved C8 and C34 involved in the covalent linkage of two neighboring protomers. In addition, a cysteine triad (C53, C94 and C135) specific of Kinetoplastid G6PDHs proved critical for stabilization of *Tc*G6PDH active site. Based on the structural and biochemical data, we posit that the N-terminal region and the catalytic site are highly dynamic. The unique structural features of *Tc*G6PDH pave the way toward the design of efficacious and highly specific anti-trypanosomal drugs.

Introduction

The diseases caused by several species of the genera *Trypanosoma* and *Leishmania* are among the most prevalent and devastating zoonotic infections in tropical and subtropical regions of the world. In the Americas, *Trypanosoma cruzi* is responsible for Chagas disease, typically evolving into a highly disabling chronic form that compromises vital organs (e.g., heart, digestive tract). The infective form of this parasite (trypomastigote) must withstand the action of harmful reactive oxygen and nitrogen species produced by the mammalian host's immune system. Within the host, the parasite invades many different cell types, differentiating into the proliferative intracellular amastigote form. Protection against host-borne radicals and oxidants, as well as the parasites' proliferation, both require for the supply of reducing power in the form of NADPH [1,2]. To fulfill this demand, the pathogen expresses several $NADP^+$-linked dehydrogenases that are developmentally regulated [3–7]. Among them, glucose-6-phosphate dehydrogenase (G6PDH) plays a housekeeping role in the generation of NADPH in trypanosomes [4,8].

Table 1. X-ray diffraction data processing and model refinement statistics

	TcG6PDHΔN37—free enzyme (apo)	TcG6PDHΔN37—in complex with Glc-6-P (G6P)
Data collection and processing		
Wavelength (Å)	1.000	1.000
Space group	$P2_1$	$P2_1$
Cell parameters		
a b c (Å)	96.6, 133.0, 107.8	96.8, 133.0, 107.7
α β γ (°)	90.0, 100.1, 90.0	90.0, 100.3, 90.0
Resolution range (Å)	29.629–2.850 (3.00–2.85)[a]	67.36–3.35 (3.53–3.35)[a]
Unique reflections	62,028 (9028)	38,508 (5606)
Completeness (%)	99.1 (99.2)	99.5 (99.9)
Multiplicity	3.5 (3.7)	3.5 (3.6)
R_{merge}[b]	0.14 (0.50)	0.21 (0.45)
R_{pim}[c]	0.09 (0.32)	0.13 (0.28)
Mean $I/\sigma(I)$	7.1 (2.3)	5.5 (2.9)
$CC_{1/2}$	0.984 (0.797)	0.959 (0.837)
Refinement		
Resolution range (Å)	29.63–2.85	34.16–3.35
Number of reflections used (working set/free set)	60,752/1257	37,660/796
R_{cryst}/R_{free}[d]	0.204/0.249	0.205/0.254
Wilson *B*/average *B* (Å^2)	61.2/44.3	50.7/36.6
Number of refined atoms (protein/ligand/water)	15,441/263/75	15,634/270/47
RMSD bond length (Å)	0.01	0.01
RMSD bond angle (°)	1.2	1.2
Estimated coordinate error DPI based on R_{free} (Å)	0.3	0.5
Ramachandran plot (% residues in favored regions/outliers)	94.43/0.36	92.21/0.91

[a] Values in parentheses are for highest-resolution shell.
[b] $R_{merge} = \Sigma_{hkl}\Sigma_i | I_i - <I>| / \Sigma_{hkl}\Sigma_i I_i$. I_i is the intensity of the i^{th} observation of reflection *hkl*, $<I>$ is the mean intensity of all observations of reflection *hkl*, summation Σ_{hkl} extends over all reflections (*hkl*), summation Σ_i is taken over all observations of each reflection (*i*), respectively.
[c] $R_{pim} = \Sigma_{hkl}[n/(n-1)]^{1/2}\Sigma_i | I_i - <I>| / \Sigma_{hkl}\Sigma_i I_i$. *n* is the multiplicity for each reflection *hkl*; other variables as defined for R_{merge}.
[d] $R = \Sigma_{hkl} | F_o - F_c | \Sigma_{hkl} F_o$. R_{cryst} and R_{free} were calculated using the working and test *hkl* reflection sets, respectively.

G6PDH catalyzes a two-electron oxidation of glucose 6-phosphate (G6P) and reduction of $NADP^+$, producing 6-phosphogluconolactone (6PGL), NADPH and H^+ [9].

$$NADP^+ + G6P \rightleftharpoons 6PGL + NADPH + H^+ \quad \Delta G'^{\circ} = -2.3 \pm 2.6\ kJ/mol \qquad (1)$$

G6PDH is the first enzyme from the oxidative branch of the pentose phosphate pathway (PPP), a pathway that also provides essential nucleotide precursors and phosphorylated sugar intermediates [10,11]. The PPP has been shown to be operative in epimastigotes of *T. cruzi* [4,12], and all the enzymes of the pathway are present in the four major developmental stages of the parasite [12]. Higher glucose consumption via the PPP and increased levels of G6PDH have been associated with higher virulence and parasite infectivity [4,12–16]. In fact, the content of G6PDH is higher in the clinically relevant stages of *T. cruzi,* and its enzymatic activity increased upon oxidative insult [14]. G6PDH has been shown to be essential for *in vitro* survival of *Trypanosoma brucei* [8] and to confer *Leishmania* increased protection toward reactive oxygen species [16] and resistance against several drugs in clinical use [17]. Overall, these are overwhelming pieces of evidence pinpointing G6PDH as an attractive anti-trypanosomatid drug target [18,19].

G6PDH from different trypanosomatid species share similar kinetic constants [14,20–22], indicating a conserved core of catalytic and ligand-binding amino acid residues. Interestingly, the *T. cruzi* enzyme (*Tc*G6PDH) is inhibited by its product NADPH and also inactivated by reducing agents [14], but the mechanism of this redox-based regulation is still unknown. A truncated form of *Tc*G6PDH, lacking the first 37 amino acids (Δ37N-*Tc*G6PDH), had previously been crystallized by our group [23].

We have now determined the crystal structures of free *Tc*G6PDH (PDB 6D23), as well as bound to the substrate G6P (PDB 6D24). *Tc*G6PDH displayed a tetrameric architecture, in contrast with previous reports [14], that claimed *Tc*G6PDH to be a dimer as most G6PDH homologs from different species [24–28]. More recently, the crystal structure of a shorter deletion mutant (Δ57N-*Tc*G6PDH) in complex with G6P and NADPH was also reported [29].

We now performed an in-depth comparative analysis between *Tc*G6PDH and the human counterpart, providing with structural and functional evidence of unique, parasite-specific, molecular features. Integrating our crystallographic, enzymatic and mutagenesis data, we propose a new model for the structural role of charged residues located in the dimer–dimer interface and for the redox-dependent allosteric regulation of *Tc*G6PDH by N-terminal cysteines, and establish a rational framework for the design of drug candidates targeting this enzyme.

Results and Discussion

Crystal structure of Δ37N-*Tc*G6PDH

Expression of Δ37N-*Tc*G6PDH resulted in crystals that diffracted X-rays substantially better than the full-length form (*Tc*G6PDH$_L$), allowing for the three-dimensional structure of Δ37N-*Tc*G6PDH to be solved. We had previously reported on the crystallization conditions of Δ37N-*Tc*G6PDH [23], both free and in complex with G6P. Both crystal structures were now determined by X-ray diffraction and refined to 2.85 Å (PDB 6D23) and 3.35 Å (PDB 6D24) resolution, respectively (Table 1). Both corresponded to the same monoclinic crystal form, with four molecules in the asymmetric unit (Fig. 1a), and G6P clearly visible in electron density for the complexed variant. *Tc*G6PDH is a tetramer that can be well described as a dimer of dimers, with each dimer burying a significantly larger solvent-exposed surface between protomers than that between dimers: the intra-dimeric interface (~5500 Å^2) engages ~10.5% of the surface of each separate protomer, whereas the smaller inter-dimeric area (~4000 Å^2) corresponds to ~4% of each dimer's surface. Both dimers are positioned in a back-to-back orientation forming the tetramer. After we released these structures in the PDB, a tetragonal crystal structure of *Tc*G6PDH was reported (PDB 5AQ1) [29], corresponding to a shorter truncated form lacking the first 57 N-terminal residues. Apart from the distinct crystal packings, our structures share identical tetrameric architecture as the tetragonal form, with slight differences in terms of inter-dimer symmetry: the tetragonal form displays only three protomers per asymmetric unit.

The point group symmetry of the Δ37N-*Tc*G6PDH tetramer is 222, identical to that of the human enzyme (*Hs*G6PDH, PDB 1QKI) [30]. The crossing angle of the two major dimer axes (i.e., axes that connect the centroids of the two protomers in each dimer) is ~40° in Δ37N-*Tc*G6PDH (Fig. 1b) compared to ~30° in *Hs*G6PDH, unveiling a substantial orientation rearrangement of the dimer of dimers

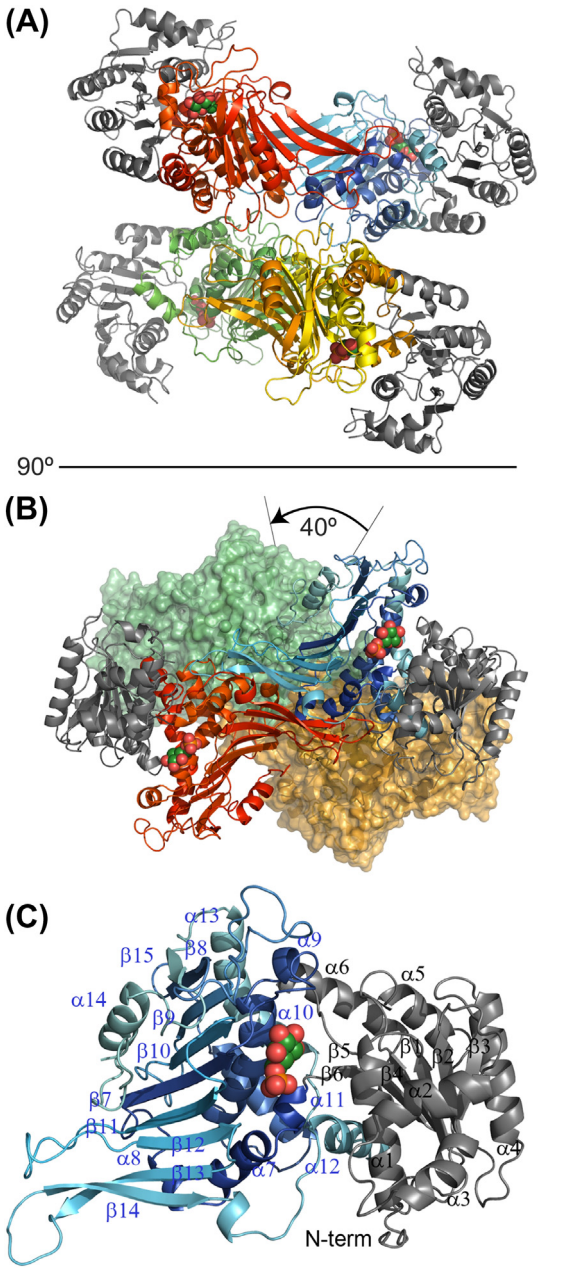

Fig. 1. Three-dimensional structure and oligomeric organization of G6P-bound Δ37N-*Tc*G6PDH. (a) Cartoon representation of Δ37N-*Tc*G6PDH tetramer with. (b) Top view displaying the 40° angle difference between dimers' axes (dimer 1, conformed by chains A and D, is shown in cartoon, and dimer 2, chains B and C, in surface representation). (c) Monomer with bound G6P. The elements conforming the secondary structure of TcG6PDH are numbered accordingly. For all figures, the N-terminal Rossmann-fold domain is colored in dark gray, whereas the C-terminal domain is shown with different colors according to the subunit (blue, chain A; green, chain B; yellow, chain C; and red, chain D). G6P atoms are depicted as spheres without hydrogens (green, carbon; red, oxygen; and orange, phosphate).

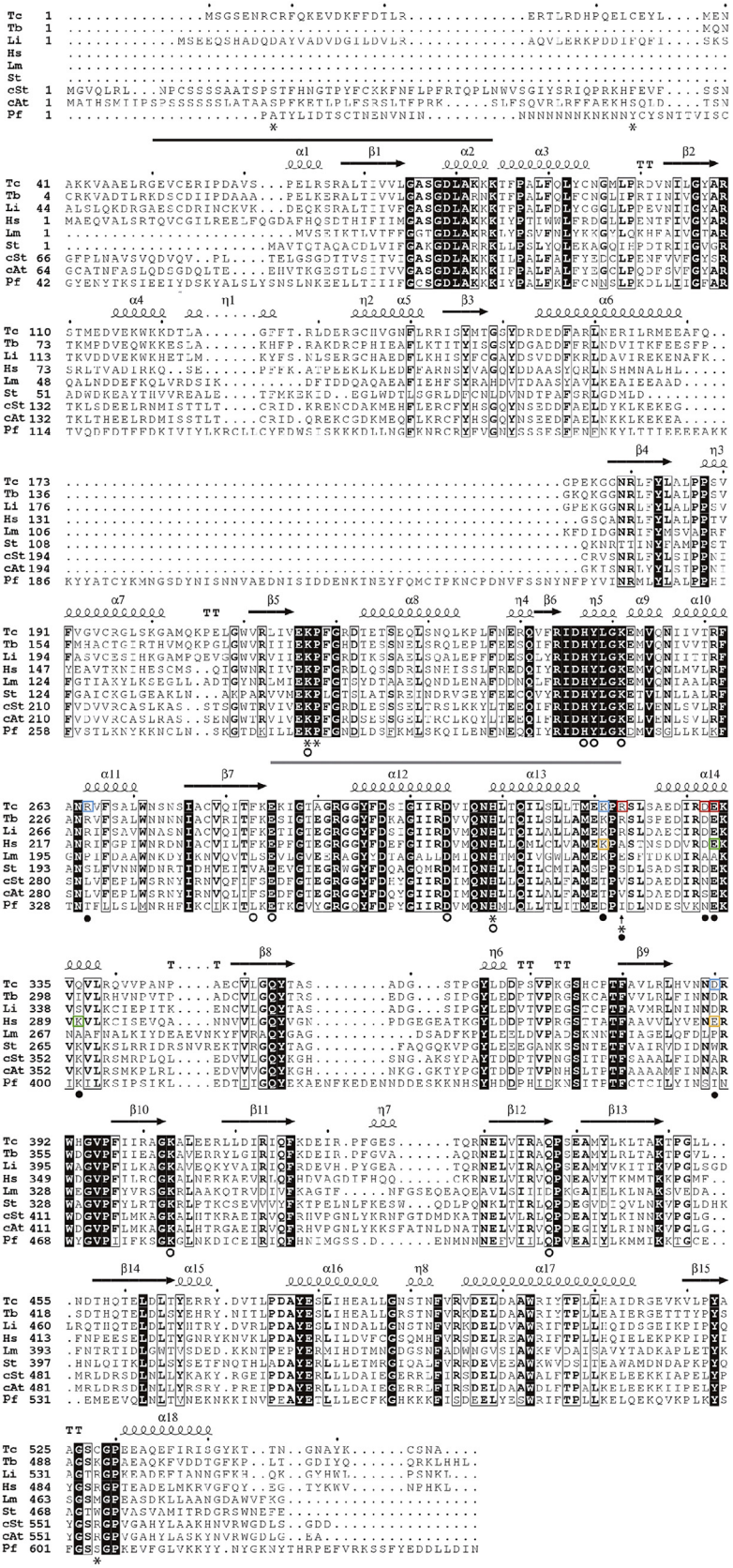

Table 2. Apparent kinetic parameters for different versions of recombinant *Tc*G6PDH

*Tc*G6PDH[a]	G6P			NAP		
	K_m (μM)	k_{cat} (s^{-1})	k_{cat}/K_m ($\mu M^{-1}.s^{-1}$)	K_m (μM)	k_{cat} (s^{-1})	k_{cat}/K_m ($\mu M^{-1}.s^{-1}$)
WT	77 ± 20	62 ± 3	0.81	16 ± 3	52 ± 2	3.3
R323G	504 ± 66	4.8 ± 0.1	0.0095	69 ± 9	5.7 ± 0.2	0.08
R323G/C528R	105 ± 22	1.10 ± 0.04	0.01	21 ± 4	1.70 ± 0.05	0.07
C528R	70 ± 13	63 ± 2	0.87	25 ± 5	72 ± 2	2.9
WT + DTT	318 ± 49	108 ± 4	0.34	39 ± 6	82 ± 3	2.1
Δ37N	275 ± 115	154 ± 16	0.56	18 ± 5	121 ± 6	6.7
C8S	332 ± 32	56 ± 1	0.17	80 ± 6	59 ± 1	0.73
C8S/C34S	98 ± 11	81 ± 2	0.82	84 ± 7	92 ± 2	1.1
C34S	130 ± 9	88 ± 2	0.68	50 ± 6	92 ± 2	1.8
C53S	1545 ± 277	2.9 ± 0.2	0.0019	>334 ± 86	2.1 ± 0.2	0.0063
C94S	178 ± 92	1.1 ± 0.1	0.0062	>622 ± 360	2.1 ± 0.6	0.0034
C135S	679 ± 105	64 ± 3	0.094	>610 ± 114	95 ± 8	0.156
H309G	185 ± 33	0.19 ± 0.01	0.001	18 ± 5	0.15 ± 0.01	0.01
P218V	123 ± 16	0.35 ± 0.01	0.003	9 ± 1	0.23 ± 0.01	0.03
K217I	226 ± 34	6.5 ± 0.3	0.029	9 ± 1	4.4 ± 0.1	0.49

[a] The different forms of TcG6PDH evaluated correspond to the following: WT, *Tc*G6PDH$_L$; WT + DTT, *Tc*G6PDH$_L$ assayed in the presence of DTT (5 mM); Δ37N, N-terminal truncated mutant of *Tc*G6PDH; C8S, C34S, C8S/C34S, C53S, C94S, C135S, C528R, R323G, R323G/C528R, P218V, H309G and K217I are point mutants of *Tc*G6PDH$_L$. The values are expressed as the mean ± SD ($n \geq 3$).

organization. Superimposing separately each dimer of both enzymes also reveals an approximate 20° rotation of one protomer with respect to the other in both dimers, whereas the intra-protomer variations superimposing 473 Cα positions are all much smaller, with pairwise figures of 1.8–1.9 Å rmsd. Thus, the tetramerization of the trypanosomal protein does not entail substantial structural changes at the subunit level. The *Tc*G6PDH inter-protomer buried surface engages extensive hydrophobic and electrostatic contacts between subunits. The inter-dimer interface displays slightly larger contributions from the crossing protomers (~500 Å^2) compared to the two pair of monomers on the same side (~370 Å^2). The interdimer interface is stabilized mainly by polar contacts (eight salt bridges and nine hydrogen bonds). It is worth highlighting that *Hs*G6PDH reveals similar inter-protomer interfaces stabilizing each dimer, but a very different inter-dimer surface, smaller (~1200 Å^2) than that of *Tc*G6PDH, and with more limited interactions between crossed (~350 Å^2) and side-by-side (~270 Å^2) protomers.

*Tc*G6PDH displays the expected tertiary structure of G6PDHs (Fig. 1c), which has been described before [29], comprising an N-terminal coenzyme-binding domain (residues 1–246) and a C-terminal domain involved in subunit dimerization (residues 251–555; Fig. 2). The two domains are connected by a one-turn 3_{10}-helix (residues 247–249). The electron density corresponding to residues 38–51 is not visible in any of the subunits on the two crystal structures, suggesting that this region is highly flexible. Comparison of the free form of Δ37N-*Tc*G6PDH to the one complexed with the G6P substrate reveals insignificant overall differences, with ~0.8 Å rmsd in all 332 Cα positions within secondary structure elements. Only minor local shifts are observed in solvent-exposed loops.

*Tc*G6PDH$_L$ forms highly stable tetramers in solution

Human G6PDH exhibits a dynamic equilibrium between an enzymatically inactive monomeric species, with active dimeric and tetrameric forms (the

Fig. 2. Multiple-sequence alignment of selected glucose-6-phosphate dehydrogenases from different phyla. Shown G6PDH sequences correspond to *Trypanosoma cruzi* (Tc; acc. no. Q1WBU6), *Trypanosoma brucei* (Tb; acc. no. Q9GRG7), *Leishmania infantum* (Li; acc. no. A2CIJ8), *Homo sapiens* (Hs; acc. no. P11413), *Leuconostoc mesenteroides* (Lm; acc. no. P11411), *Salmonella typhimurium* (St; acc. no. Q8ZNW2), chloroplastic *Solanum tuberosum* (cSt; acc. no. Q43839), chloroplastic *Arabidopsis thaliana* (cAt; acc. no. Q43727) and *Plasmodium falciparum* (Pf; acc. no. Q8IKU0). Strictly conserved residues are highlighted with black background, while those conserved in at least seven out of nine sequences are shown in bold letters. The secondary structure elements of Δ37N-*Tc*G6PDH with bound G6P (PDB 6D24) are displayed above the sequence alignment. The black and gray lines indicate the N-terminal V52–K84 and E285–R323 regions that may play an allosteric role in *Tc*G6PDH activity. At the bottom of the alignment, the black circle, the empty circle, the asterisk and the arrow indicate residues involved in ionic interactions to stabilize the dimer–dimer contacts, mutated in this study, interacting with G6P and the position of R323, respectively. Residues participating in dimer–dimer salt bridges in *Tc*G6PDH are framed in red (R323–D332 and R323–E333) and light blue (R265–D390 and K321–D390), and those for *Hs*G6PDH are framed in yellow (K275–E347) and green (K290–E287).

dimer being the predominant arrangement), an equilibrium that is influenced by the environment's physicochemical properties and presence of ligands [31]. For instance, $NADP^+$ and G6P stabilize, respectively, the dimeric and monomeric forms of *Hs*G6PDH [32,33]. In contrast, the oligomeric state adopted by the active form of *Tc*G6PDH is still a matter of debate, with evidence favoring a dimeric organization [14] contrasting with reports of *Tc*G6PDH forming stable tetramers in physiological buffer solutions and in crystals [23,29]. To further explore about the relevant quaternary structure of the trypanosomatid enzyme, *Tc*G6PDH$_L$ was subjected to size exclusion chromatography (SEC) in the presence of saturating substrate concentrations ($NADP^+$ or G6P; see the kinetic parameters in Table 2). The SEC profiles of *Tc*G6PDH$_L$ did not change significantly in the presence or absence of ligands (Fig. 3a), always displaying a very stable tetrameric configuration. Dehydroepiandrosterone, a G6PDH inhibitor [22], was also assayed, revealing no detectable alteration of *Tc*G6PDH$_L$'s SEC migration. Beside the action of specific ligands or substrates, it is known that *Hs*G6PDH dimers are stabilized by increasing ionic strength or removal of Mg^{++} [32]. Again contrasting the human enzyme's properties, *Tc*G6PDH$_L$ tetramers were refractory to high ionic strength or to the absence of Mg^{++} (Fig. 3b). Covalent interactions stabilizing the tetrameric organization of the trypanosomal G6PDH were also ruled out, given that no species of low molecular mass were detected under reducing conditions (Fig. 3b).

In sum, *Tc*G6PDH$_L$ forms highly stable tetramers associated through non-covalent interactions, in contrast to the human enzyme's properties (Fig. S2).

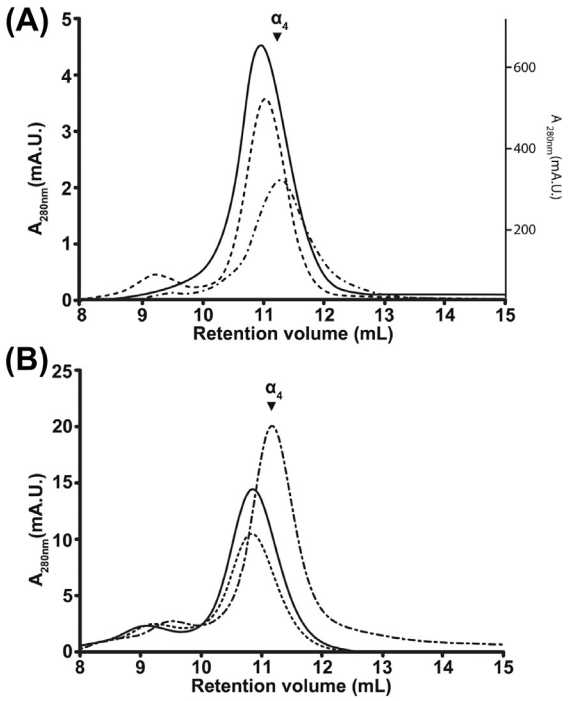

Fig. 3. SEC analysis of recombinant *Tc*G6PDH$_L$. Full-length G6PDH (0.8–2.4 μM) was gel filtrated on a Superdex G200 resin (10/300 column) pre-equilibrated in reaction buffer [Tris 50 mM (pH 7.5), NaCl 0.5 M and $MgCl_2$ 5 mM] containing saturating concentrations of different ligands. (a) DHEA 100 μM (dotted line; retention volume, rv, of 11.2 mL ≅ 240 kDa), $NADP^+$ 5 mM (dash-dotted line, rv = 11.3 mL ≅ 230 kDa) or G6P 5 mM (black line, rv = 10.8 mL ≅ 286 kDa). (b) Reaction buffer lacking magnesium (dotted line, rv = 10.8 mL ≅ 286 kDa), with DTT 5 mM (black line, rv = 11.2 mL ≅ 240 kDa) or NaCl 1 M (black dash-dotted line, rv = 11.2 mL ≅ 240 kDa). For both plots the arrowhead indicate the position at which the peak of the non-treated *Tc*G6PDH$_L$ elutes in reaction buffer (control, rv = 11.2 mL ≅ 240 kDa). Representative chromatograms ($n \geq 2$) are shown for each condition. For panel A, the right *Y*-axis scale corresponds to the sample run in the presence of G6P, while the left *Y*-axis scale corresponds to the samples run in the presence of DHEA and $NADP^+$.

*Tc*G6PDH R323 is a key determinant for tetramerization

The dimer–dimer interface of *Tc*G6PDH reveals eight ionic bonds (Fig. 4a): R323–D332′, AR323–E333′, R265–D390′, K321–D390′, D390–R265′, D390–K321′, D332–R323′ and E333–R323′ (the prime symbol identifies residues within the neighboring dimer, chain A of dimer 1 interfaces with chain C in dimer 2, and the same range of interactions can be identified between dimer 2's chain B and dimer 1's chain D). Although similarly charged residues occupy equivalent positions in *Hs*G6PDH (Fig. 2), only four of them are engaged in forming salt bridges: K275–E347′ (K321–D390′ in *Tc*G6PDH) and E287–K290′ (E333–Q336′ *Tc*G6PDH; note that the salt bridge is absent in the latter case, since K290 is substituted by Q336 in the trypanosomal enzyme). Moreover, a comparison of the tetrameric configurations of these proteins reveals that, due to the shift in relative orientations, the pair R219–E347′ of *Hs*G6PDH is separated by 7 Å, whereas the side-chain groups of the equivalent residues in *Tc*G6PDH (R265–D390′) are only 2.8 Å apart and hence at a suitable distance for ionic interaction. More importantly, the substitution of R323 by an alanine (A277) eliminates all at once four salt bridges in the human enzyme. R323 in *Tc*G6PDH is located within a loop connecting helices α13 and α14, interacting with both D332 and E333 in helix α14 from the neighboring dimer. As a means to verify the relevance of the ionic bonds in holding the dimers together within the tetramer, *Tc*G6PDH$_L$ was resolved by SEC at lower pH (5.5). Under such condition, the major species eluted with a lower apparent molecular mass compared to the same sample analyzed at pH 7.5 (Fig. 4b), strongly suggesting partial dissociation of the tetramer. We next replaced R323 by a glycine using genetic

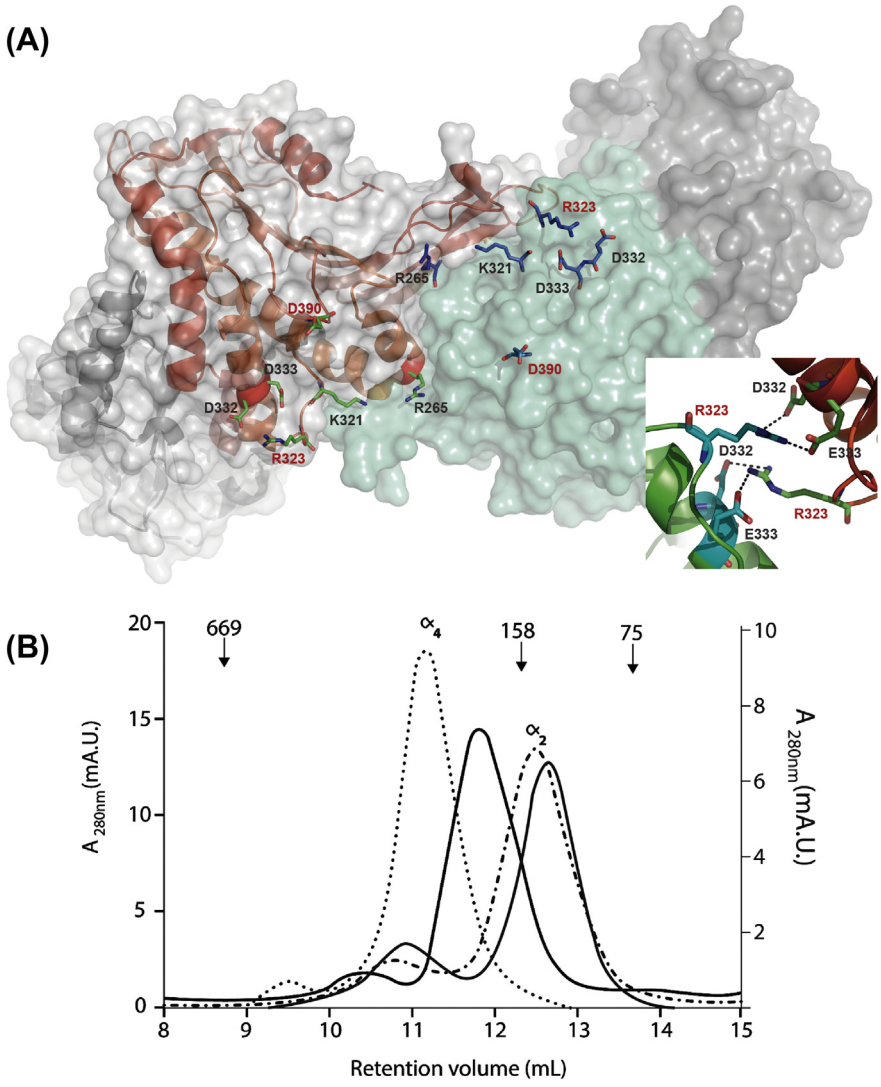

Fig. 4. Tetrameric interface of *Tc*G6PDH. (a) Critical residues involved in salt bridges between dimers are shown in green sticks (chain A with transparent surface and backbone shown as cartoon with N- and C-terminal domains colored in black and red, respectively) and blue sticks (chain D shown as surface with N and C-terminal domain colored in gray and pale green, respectively) sticks. Residues non-conserved in *Hs*G6PDH are labeled in red (R323 and D390). The inset shows with greater detail the salt bridges formed between R323 and D332 and E333 from subunits A and B (green and red cartoon backbone). (b) *Tc*G6PDH$_L$ was gel filtrated on a Superdex G200 (10/300 column) equilibrated at pH 7.5 (dotted line; rv 11.2 mL ≅ 240 kDa) and pH 5.5 (black line; rv = 11.8 mL ≅ 168 kDa). The R323G *Tc*G6PDH$_L$ mutant was separated in the same column equilibrated in reaction buffer without DTT (dash-dotted line; rv = 12.5 mL ≅ 135 kDa) and with DTT 5 mM (dark gray line; rv = 12.7 mL ≅ 124 kDa). The arrows indicate the position of the peaks corresponding to the molecular weight standards used for column calibration (thyroglobulin 669 kDa, aldolase 158 kDa and albumin 75 kDa). α_4 and α_2 indicate the expected elution volumes for the tetrameric and dimeric species of TcG6PDH$_L$. A representative chromatogram (n ≥ 2) for each condition is shown. The left *Y*-axis scale corresponds to the sample run at pH 7.5 (dotted line), whereas the right *Y*-axis scale refers to the other samples.

engineering, and the point-mutated protein (*Tc*G6PDH$_L$-R323G) now behaved as a pure dimeric species in SEC (Fig. 4b). Such elution pattern did not change under reducing conditions, further supporting that covalent interactions do not contribute to the dimeric assemble of the protein.

A positively charged residue at position 323 is strictly conserved in all G6PDH enzymes from kinetoplastid protozoa (with Arg largely prevailing over Lys) with the sole exceptions of the non-pathogenic *Leishmania enrietti*, *Crithidia fasciculata* and *Leptomonas* spp., which possess a Gln/Asn/Ser (Fig. S1). Moreover, the pair D332/E333 is equally conserved. The absence of a positively charged residue occupying position 323 in orthologues from other lineages (Fig. 2) suggests that these proteins

will not form stable tetramers. In order to verify this hypothesis, recombinant G6PDH from *C. fasciculata* (*Cf*G6PDH$_L$), which presents an asparagine residue (N325) substituting the otherwise conserved R323 of *Tc*G6PDH, was subjected to SEC. Under reducing [5 mM dithiotreitol (DTT)] conditions and 0.5 M NaCl, *Cf*G6PDH$_L$ eluted with an apparent molecular weight of ~260 kDa, consistent with the protein being a tetramer (the sequence-derived molecular weight of the His-tagged *Cf*G6PDH$_L$ monomer is 65 kDa). At a higher ionic strength (1 M NaCl), most of *Cf*G6PDH$_L$ still eluted as a tetrameric species, with a minor peak corresponding to the monomer (68 kDa apparent molecular weight). At pH 6.5, which is one unit higher than that required to dimerize *Tc*G6PDH$_L$ (pH 5.5; Fig. 4b), *Cf*G6PDH$_L$ eluted as a broad peak, with a maximum corresponding to the dimer (~118 kDa) (Fig. 5a). This behavior is consistent with the hypothesis described above, indicating that fewer or weaker electrostatic interactions are stabilizing the dimer–dimer interaction in *Cf*G6PDH$_L$, compared to *Tc*G6PDH. However, in contrast to *Hs*G6PDH that also lacks R323 and is predominantly dimeric (Fig. S2), *Cf*G6PDH$_L$ proved to be tetrameric, suggesting that residues other than R323 might also contribute to stabilize the quaternary structure of the protein. Structural analysis of *Cf*G6PDH$_L$ (using a homology-based model generated with *Tc*G6PDH PDB 6D24 as the template) anticipates R331 (close to N325) to be well located to establish a salt bridge with D334 (equivalent to *Tc*G6PDH D332) from a neighboring

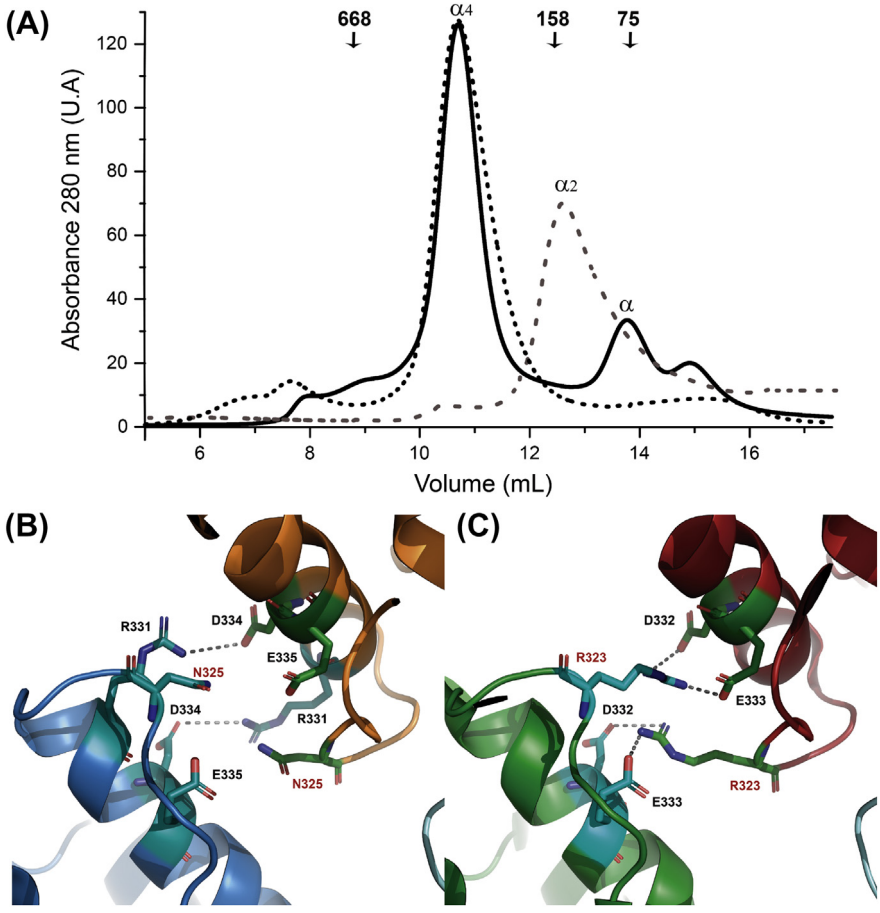

Fig. 5. G6PDH from *C. fasciculata* forms less stable tetramers than the trypanosomal homolog. (a) SEC analysis of recombinant *Cf*G6PDH$_L$. *Cf*G6PDH$_L$ (24 uM) was reduced (5 mM DTT, 15 min) and gel filtrated on a Superdex G200 resin (10/300 column) pre-equilibrated in reaction buffer [Tris 50 mM (pH 8), NaCl 0.5 M and $MgCl_2$ 5 mM] containing DTT 5 mM (black dotted line, major peak at rv = 10.7 mL ≈ 258 kDa) or NaCl 1 M (black line, major peaks at rv = 10.7 mL ≈ 258 kDa and rv = 13.7 mL ≈ 68 kDa), or in buffer MES pH 6.5 and -NaCl 0.5 M (dotted gray line rv = 12,6 ≈ 118 kDa). Residues participating in the formation of the additional salt bridge between dimers in G6PDH from (b) *C. fasciculata* and (c) *T. cruzi*. In *Cf*G6PDH, an asparagine residue (N325) substitutes the otherwise conserved arginine (R323 in *Tc*G6PDH) present in G6PDH from trypanosomatids, hence precluding the formation of a double salt bridge with the highly conserved D334 and E335 (D332 and E333 in *Tc*G6PDH) from a vicinal subunit. Nonetheless, nearby R331 in *Cf*G6PDH is anticipated to be at a suitable distance to establish a compensatory ionic bond with D334.

dimer (Fig. 5b). We speculate that this R331–D334′ salt bridge in *Cf*G6PDH$_L$ may partially compensate for the stabilizing effect of the two salt bridges R323–D332′ and R323–E333′ in *Tc*G6PDH$_L$ (Fig. 5c). Taken together, our data lead us to posit that all kinetoplastids G6PDH bearing the R323–D332/E333 salt bridges will likely form stable tetramers.

Structural role of R323 in *Tc*G6PDH enzymatic activity

Compared to wild-type *Tc*G6PDH$_L$ (99 U/mg), the specific activity of the dimeric R323G mutant (32 U/mg) was 68% lower, indicating that alteration of quaternary structure impairs enzymatic activity. Kinetic characterization of the R323G mutant revealed a 4- and 7-fold increase in K_m^{app} for $NADP^+$ and G6P, respectively, compared to the wild-type enzyme (Table 2). Furthermore, the point-mutant displayed 85- and 41-fold lower apparent catalytic efficiencies for G6P and $NADP^+$, respectively (Table 2), indicating that the dimer also catalyzes the enzymatic reaction slower. Therefore, R323 appears to be allosterically connected to the active site.

An allosteric binding site for $NADP^+$ toward the C-terminal portion of the *Hs*G6PDH dimerization domain has been reported to stabilize its active, dimeric form [30,34]. In fact, *Hs*G6PDH mutants such as R393G or R393H, isolated from clinical cases and displaying impaired binding of allosteric $NADP^+$, are remarkably unstable and show 2.5- to 13-fold increase of the K_m^{G6P} (and a minor 1.3-fold increase of K_m^{NADP+}) when compared to the wild-type enzyme [33,35]. The protein main-chain trace and several key NADP-binding residues are conserved between the human and *T. cruzi* enzymes in this region [29]. However, *Tc*G6PDH displays substitutions in three positions among the critical amino acids that bind the adenosine moiety: Y503, K366 and R487 in *Hs*G6PDH [36] are replaced respectively by T544, L409 and C528 in *Tc*G6PDH (Fig. 6a). This raises the question as to whether structural $NADP^+$ may bind and stabilize dimeric *Tc*G6PDH in a catalytically competent conformation. To address this point, the structural $NADP^+$-binding site of *Hs*G6PDH was partially reconstituted in the *Tc*G6PDH$_L$ R323G mutant by substituting C528 for an arginine (C528R). There is a second reason for choosing to mutate this site, besides the fact that the basic residue R487 (occupied by C528 in *Tc*G6PDH) is critical for non-catalytic $NADP^+$-binding in the human enzyme [30,36] (Fig. 2). In *Tc*G6PDH$_L$, C528 is forming an intramolecular disulfide with C552 (chains A and B) or harbors a negative charge due to oxidation of its sulfur atom to a sulfenic acid (chains C and D) (Fig. 6a), according to crystallographic data for Δ37N-*Tc*G6PDH in complex with G6P. In consequence, binding of structural $NADP^+$ to this site in *Tc*G6PDH would be impaired by steric or electrostatic effects. Interestingly, the *Tc*G6PDH$_L$ double mutant R323G-C528R displayed K_m^{app} figures for $NADP^+$ and G6P that are very similar to those of the wild-type enzyme, and k_{cat} values as low as those of the single R323G mutant (Table 2).

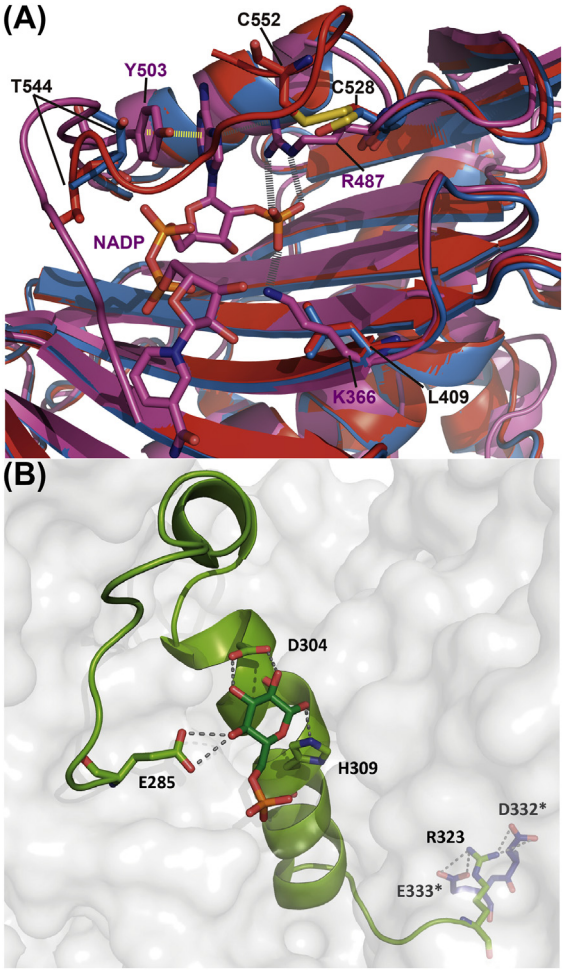

Fig. 6. Structural $NADP^+$ binding-site and catalytic elements linked to R323 in *Tc*G6PDH. (a) Region involved in binding allosteric $NADP^+$ in human G6PDH (PDB 1QKI; chain A, backbone and ligand shown in magenta) [29,33]. Superimposed is shown the backbone structure of the chain A (red) and chain D (blue) from Δ37- N-*Tc*G6PDH. The residues that participate in $NADP^+$ binding in *Hs*G6PDH (K366, R487 and Y503) and are not conserved in *Tc*G6PDH (L409, C528 and T544) are depicted as sticks colored according to the respective backbones. Polar interactions are depicted with gray dashed lines, and π-stacking with yellow dashed lines. The C528–C552 disulfide and the C528 sulfenic seen in the crystal structure of Δ37 N-*Tc*G6PDH (PDB 6D24) are shown as sticks. (b) Surface representation of *Tc*G6PDH (PDB 6D24, chain A) with backbone elements of the segment E285–R323 displayed as a green cartoon. Residues playing key roles in G6P-binding (D304 and E285) or catalysis (H309) are shown as sticks. R323 is also shown interacting electrostatically to the neighbor protein´s D332 and E333 (in blue sticks).

Altogether, this strongly suggests that partial reconstruction of the structural site for $NADP^+$ in dimeric *Tc*G6PDH$_L$ restores substrates' binding, but not the active conformation of the enzyme.

Detailed inspection of the *Tc*G6PDH structure provides clues about the structural role of R323 in building the enzyme's active site. R323 is located within a loop that is contiguous to structural elements (from E285 to R323) engaged in G6P-binding (e.g., E285 and D304) and catalysis (H309) (Figs. 2 and 6b; see Table 2). The packing effect of the inter-dimer salt bridges between R323 and D332/E333 stabilizes the R323-containing loop and the preceding structural elements that are part of the active site (β7-α12 loop and helices α12 and α13). In the R323G mutant, such a stabilizing effect is lost, leading to lower K_m^{app} values and a catalytically non-competent conformation of the active site.

In sum, our results support the notion of a bidirectional coupling between the active site and the tetramerization surface in *Tc*G6PDH, and that the tetrameric structure of *Tc*G6PDH surrogates the active site-stabilizing role of the second, non-catalytic $NADP^+$-binding site, otherwise naturally present in dimeric G6PDHs.

Cysteine 8 and 34 within the N-terminal extension of *Tc*G6PDH form intra-dimer disulfide bridges

Previous work had shown that recombinant and native *Tc*G6PDH$_L$ are inactivated by treatment with mM concentrations of DTT and/or GSH, while Δ37N-*Tc*G6PDH is unaffected [14]. This suggests that cysteine residues within the N-terminal extension of *Tc*G6PDH$_L$ might be forming a covalent bond(s) modulating enzymatic activity. As a first approach to elucidate whether the posited disulfide bond(s) is intra- or inter-molecular, different versions of *Tc*G6PDH were subjected to sodium dodecyl sulfate–polyacrylamide gel electrophoresis (SDS-PAGE) in the presence or absence of a reducing agent (Fig. 7a). Interestingly, under reducing

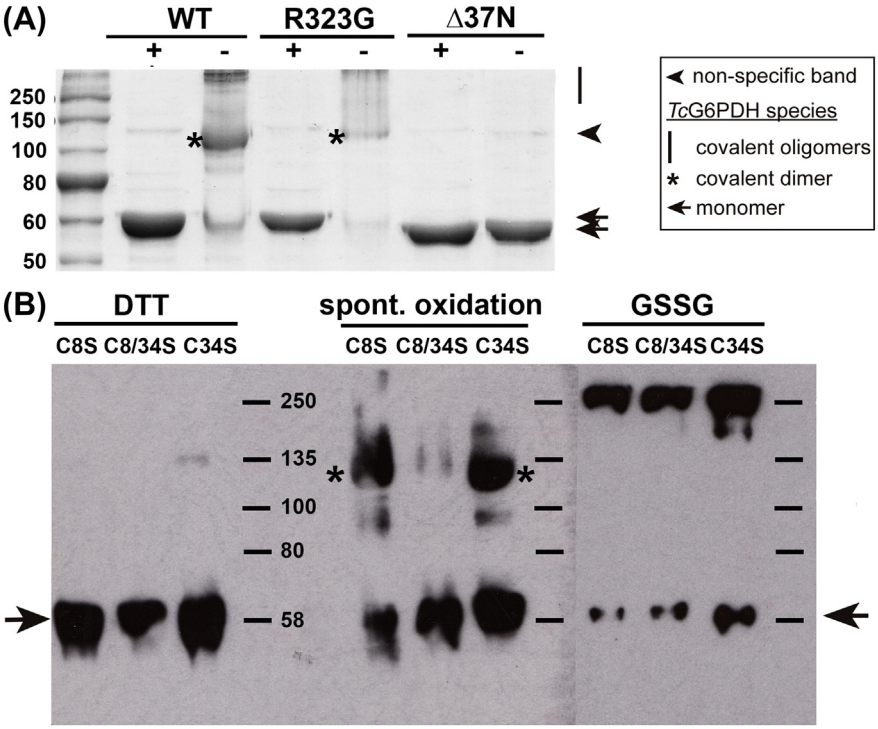

Fig. 7. Cysteines from the N-terminal extension are responsible for the formation of inter-subunit disulfides in *Tc*G6PDH$_L$. (a) SDS-15% PAGE for full-length wild type (WT) and R323G (R323G), and Δ37 N- (Δ37 N) *Tc*G6PDH run in the presence (+) or absence (–) of reducing agent (β-mercaptoethanol). (b) Western blot of C8S, C34S and the double mutant C8S/C34S (C8/34S) of *Tc*G6PDH$_L$ that were pre-reduced with 150 μM DTT (DTT) and, upon removal of excess reducing agent, further treated with 150 μM glutathione disulfide (GSSG) for 45 min or that underwent spontaneous oxidation upon storage for 1 week in the absence of a reducing agent (spont. oxidation). Protein samples (300 ng/lane) were separated on 12% polyacrylamide SDS-PAGE under non-reducing conditions. Samples treated with GSSG were run in paralell on a separate gel due to space constraints. The bands corresponding to monomeric and dimeric species are indicated with arrows and asterisks, respectively, while the region corresponding to covalent multimeric species is marked with a vertical line (in panel A). The arrow head on panel A marks a non-specific protein migrating right above the dimeric form of *Tc*G6PDH, which proved unreactive with specific anti-*Tc*G6PDH serum.

conditions, *Tc*G6PDH$_L$ migrated as a single ~60 kDa species, whereas a heterogeneous population was revealed under non-reducing conditions, with a major form of ~120 kDa that corresponds to a dimer. In contrast, Δ37N-*Tc*G6PDH showed always a single ~55-kDa form (monomeric), independent of its oxidation state, indicating that C8 and/or C34 establish inter-monomer disulfide bonds. The elution of *Tc*G6PDH$_L$-R323G as a dimer in SEC under non-reducing conditions (Fig. 3b) was indicative that the covalent bond is intra- and not inter-dimeric. Comforting this observation, under non-reducing SDS-PAGE, this mutant showed a similar migration profile to that of *Tc*G6PDH$_L$, in particular with the appearance of a band corresponding to a dimer (~120 kDa; Fig. 7a).

Next, we investigated which cysteines from the N-terminal extension participate in the formation of the covalent link between subunits of the dimer. Single (C8S and C34S) and double (C8S/C34S) *Tc*G6PDH$_L$ mutants were produced and stored for 1 week in the absence of reducing agents (time-point based on preliminary spontaneous oxidation observations), prior to Western blot analyses. For each mutant, the following samples were prepared, separated in a non-reducing SDS-PAGE and immunoblotted with anti-*Tc*G6PDH serum: (i) untreated protein (spontaneous oxidation), (ii) protein reduced with a 60-fold molar excess of DTT and (iii), upon removal of excess reducing agent, oxidized with a 60-fold molar excess of glutathione disulfide (GSSG) for 45 min. For all Cys mutants treated with DTT, the polyclonal anti-serum recognized a single species of ~60 kDa, which corresponds to the molecular weight of the *Tc*G6PDH$_L$ monomer (Fig. 7b). The monomer was also identified in the untreated samples of all Cys mutants. However, forms migrating as the dimer (~120 kDa) were also detected in the untreated C8S and C34S mutants, and not in the double C8/34S mutant. This indicates that both C8 and C34 participate in the formation of disulfide bridges between the subunits of each dimer (C8–C8′ and C34–C34′). For all *Tc*G6PDH$_L$ Cys mutants, treatment with GSSG induced almost a full conversion of the monomeric species into large-molecular-weight covalent multimers without formation of dimers as intermediate species. In conclusion, the assay shows that storage of the sample in the absence of a reducing agent produces a selective oxidation of the N-terminal cysteines, whereas GSSG triggers a non-specific oxidation of cysteines residues in *Tc*G6PDH$_L$. Overall, the formation of intra-dimeric disulfide bonds seems to be a fine-tuned redox process.

Although the thiol group(s) from the second subunit that is partnering with C8 and/or C34 remains unknown, structural analysis of *Tc*G6PDH provides some hints. *Tc*G6PDH$_L$ harbors 11 cysteine residues (four more than *Hs*G6PDH), among which only C244 occupies a shared position with the human protein (Fig. 2). In the crystal structure of Δ37N-*Tc*G6PDH, nine cysteines are observed, some of which are engaged in intramolecular disulfides (C53–C135 for PDB 6D23 and C528–C552 for PDB 6D23 and chain A and B of PDB 6D24), others are seen to be oxidized to sulfenic acid (C528 in chain C and D of PDB 6D24; Fig. 5a), buried and inaccessible to the solvent (C195, C278, C377), or located at distances incompatible to establish disulfide bonds with C8 and/or C34 (C195, C278, C349 and C377). Together with the redox Western blot data, structural constraints support the hypothesis that C8 and C34 form intra-dimer disulfide bridges.

The N-terminal extension and cysteines therein modulate *Tc*G6PDH activity

Previous studies proposed a regulatory role of the N-terminal cysteines in the activity of *Tc*G6PDH [14], based on the sensitivity of *Tc*G6PDH$_L$ but not of Δ37N-*Tc*G6PDH to inhibition by DTT and GSH. However, the molecular mechanism of such regulation remained unknown and is now partially uncovered by kinetic analysis. First, we compared the kinetic parameters for *Tc*G6PDH$_L$ determined under reducing (WT + DTT) and non-reducing conditions (WT). Partial reduction of DTT-accessible disulfide bonds impairs mainly the K_m^{app} for G6P (4-fold increase) and, to a minor extent, for $NADP^+$ (2.4-fold), while increasing the k_{cat}^{app} by ~1.7-fold (see further comments in the next section). Despite this apparent compensation, reduced *Tc*G6PDH$_L$ displays an apparent catalytic efficiency (k_{cat}^{app}/K_m^{app}) for both substrates at least 50% lower than that exhibited by the oxidized enzyme. A potential contribution of the C528–C552 disulfide bond to the kinetic behavior of reduced *Tc*G6PDH$_L$ can be ruled out, because the C528R mutant presented similar K_m^{app} and k_{cat}^{app} values to the WT + DTT sample (Table 2). The kinetic results obtained for WT + DTT should thus be interpreted as an overall contribution of cysteines 8, 34, 53, 94 and 135 to the activity of reduced *Tc*G6PDH$_L$.

Further analysis of the C8S/34S *Tc*G6PDH$_L$ double mutant allowed to evaluate the contribution of the intermolecular disulfide to enzyme activity. Compared to the WT enzyme assayed under non-reducing conditions, the mutant presented 5-fold higher K_m^{app} for $NADP^+$ than the WT and a 3-fold lower apparent k_{cat}/K_m for this substrate. Interestingly, C8S/34S displayed on the other hand nearly identical kinetic pad with the WT enzyme's (Table 2). In agreement with this behavior, the single C8S and C34S mutants displayed ≥2-fold higher K_m^{app} and k_{cat}^{app}/K_m^{app} values for $NADP^+$. More puzzling was the role of the individual cysteines with regard to G6P. While C8S/34S and WT showed no significant

difference in K_m^{app}, C8S and C34S showed respectively 4.3- and 2.4-fold higher K_m^{app} for G6P, which translated into lower catalytic efficiencies than the WT or C8S/34S (Table 2). Worth noting, nearly half of C8S and C34S *Tc*G6PDH$_L$ are forming inter-dimer disulfide bridges, according to Western blot analyses of non-reduced samples (Fig. 7b). Thus, the kinetic parameters obtained for these single mutants represent an average estimation for redox-heterogeneous samples, suggesting that the real impact of lacking the individual Cys residues is underestimated. On the other hand, assayed under non-reducing conditions and compared to the WT enzyme, the mutant devoid of the N-terminal extension (Δ37N) presented a 3.6-fold higher K_m^{app} for G6P, similar K_m^{app} for $NADP^+$, and a 2-fold increased apparent k_{cat} (Table 2). This indicates that the N-terminal extension plays a role in sculpting the G6P-binding site.

Based on the kinetic analysis, we can conclude that the formation of interdimer disulfide bonds mediated by C8 and C34 (and intramolecular disulfides by the C53, C94 and C135 triad) favors enzymatic activity. In contrast, the formation of single inter-dimeric homo-disulfides is detrimental for G6P binding, in particular when the most N-terminal C8 is not involved in the covalent bond. Because this effect is not observed in the absence of both cysteines (C8/34S mutant), it will be interesting to probe in future studies whether the dimeric forms of C8S and C34S represent intermediate species with a not properly folded N-terminal extension impairing, in such a state, G6P binding.

The kinetoplastid-conserved cysteine triad C53, C94 and C135 has a major structural role in sculpting the $NADP^+$-binding and catalytic site in *Tc*G6PDH

*Tc*G6PDH C53, C94 and C135 are highly conserved among kinetoplastid G6PDHs (Figs. 2 and S1). According to the Δ37N-*Tc*G6PDH structure, the thiol groups of this triad are separated 2 to 9 Å from one another, with the C53–C135 pair forming a disulfide bond and C94 buried, likely hydrogen-bonded to H136. Supporting the spatial proximity and redox reactivity of these Cys residues, the structure of Δ57N-*Tc*G6PDH [29] shows a disulfide bridge bonding C94 to C135 (Fig. 8). Although the kinetic analyses presented in previous sections suggest that this Cys triad may contribute to modulating enzyme activity, information about their precise role and significance is still lacking. To gain further insight into these aspects, single Cys-to-Ser *Tc*G6PDH$_L$ mutants (C53S, C94S and C135S) were generated and their kinetic constants determined under non-reducing conditions (Table 2).

Compared to the WT enzyme, all kinetic parameters were negatively affected in the three points mutants. For instance, the K_m^{app} for $NADP^+$ shows a ≥21-fold increase for all three mutants, and the K_m^{app} for G6P is 20-, 2- and 9-fold higher for C53S, C94S and C135S, respectively. The apparent k_{cat} values for both substrates dropped between 21 to 56 times for C53S and C94S. Always comparing to WT, the C53S and C94S mutants displayed strikingly lower k_{cat}^{app}/K_m^{app} for both substrates (130- to 955-fold). For C135S, the unchanged (for G6P) or 1.8-fold increased (for $NADP^+$) k_{cat}^{app}, partially mitigated the final effect in kinetic efficiency for both substrates (8.5- and 21-fold lower for G6P and $NADP^+$, respectively). Both K_m^{app} and k_{cat}^{app}/K_m^{app} of WT G6PDH showed a similar trend when measured in the presence of DTT (5 mM), although they differed in the magnitudes. This apparent disparity is likely explained by the fact that the kinetic data for WT + DTT were obtained with a protein sample shortly exposed (<1 min) to the reducing agent, hence only partially reduced. A fully reduced protein could not be used because *Tc*G6PDH$_L$ then completely loses its activity, in line with prior studies [14] and with our observations on the detrimental effect of lacking structural/regulatory cysteines.

The Cys-triad is located within the Rossmann-fold domain, contiguous in sequence to structural elements that harbor substrate-binding amino acids (Fig. 8). Disruption of the interactions established by these cysteines likely destabilizes this important region of the protein, resulting in the kinetic consequences described above. Further crystallographic studies shall reveal the structural role of this Cys-triad residues in kinetoplastid G6PDHs.

Dynamic active site and N-terminal domain: a catalytic model of *Tc*G6PDH

The kinetic studies highlighted an important role of kinetoplastid-specific cysteine residues from the N-terminal domain of *Tc*G6PDH, in modulating enzyme activity. In order to provide with mechanistic insights on the residues and structural elements affecting the reaction catalyzed by *Tc*G6PDH, the crystal structures of N-terminally truncated proteins with bound ligands (PDB 6D24 and PDB 5AQ1) were compared to a model of the enzyme–G6P–$NADP^+$ ternary complex ("catalytic model") obtained by molecular dynamics simulations calculated over 80 ns [19]. Relative to the crystallographic structures, both substrates adopted different conformations in the catalytic model, with $NADP^+$ shifted about 3 Å toward the catalytic site and G6P being anchored almost perpendicularly and deeper into the structure core (Fig. 9a). The shift in the position of $NADP^+$ is due to movements of several elements from the Rossmann-fold domain (i.e., helix α2, and loops β1–α2, β2–α3 and β3–α6; Fig. 9a) and do not involve the gain or loss of side chain interactions. In contrast, the conformation observed for G6P in the simulation is facilitated by relaxation of the element connecting

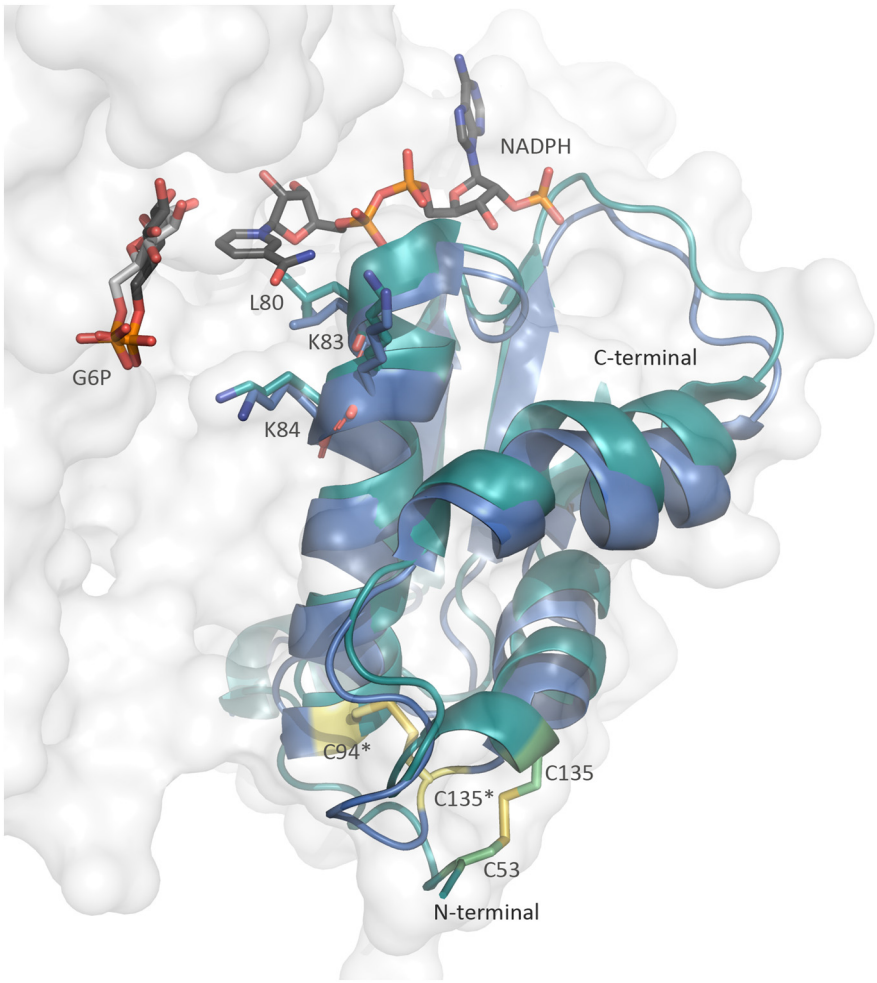

Fig. 8. Dynamics of the N-terminal region and cysteine triad of *Tc*G6PDH. Cartoon representation of the N-terminal segment of Δ37N-*Tc*G6PDH (V52–K84) (aquamarine color; chain D, PDB 6D24) and Δ57N-*Tc*G6PDH (P62–K84: blue color; chain A, PDB 5AQ1) with bound G6P and NADPH. Substrates (G6P and NADPH), residues involved in substrate binding (L80, K83 and K84) [19] and N-terminal cysteine triad (C53, C94 and C135; highlighted with an asterisk for Δ57N-*Tc*G6PDH) are shown as sticks (cyan, carbon; red, oxygen; blue, nitrogen; orange, phosphate; yellow, sulfur).

strand β6 and helix α9, namely, the linker between the N- and the C-terminal domains, and the consequent rewiring of the substrate's interaction network (Fig. 9b). In this regard, the π-stacking between Y248 and H309 is lost in the catalytic model, which may contribute to destabilize the helical structure of this segment; hence, nearby H247 is anticipated to shift 3 Å toward α9, allowing for a reorientation of the sugar moiety of G6P, itself anchored to the pocket via H-bonding with K217, H247, Y248 and H309. Because of the partially unfolded conformation of the β6–α9 linker segment, Y248 and K251 are located at unsuitable distances to interact with the phosphate group of G6P (Fig. 9c). Instead, K83 and K84 (located in α2) can interact with the substrate's phosphate (Fig. 9b), an interaction confirmed by kinetic analysis of mutants [19] but not observed in the substrate-bound crystal structures.

Another region of *Tc*G6PDH that displayed slight differences in the conformation between the crystallographic structure and the molecular dynamics model is loop β5–α8. This loop contains a proline residue (P218), which invariably adopts the *cis* isomer in all subunits of *Tc*G6PDH, both apo or holo forms (Fig. 9b and c). This differs with data reported for human and *Leuconostoc mesenteroides* G6PDH, where this proline shuttles from *trans* to *cis* upon formation of the productive ternary complex [26,36–40]. The almost exclusive role of the *cis*-Pro in the conformation of the active site was verified by an increase in 2 orders of magnitude in the apparent k_{cat} and k_{cat}/K_m for both substrates when this residue was exchanged by a valine in *Tc*G6PDH$_L$ (Table 2,

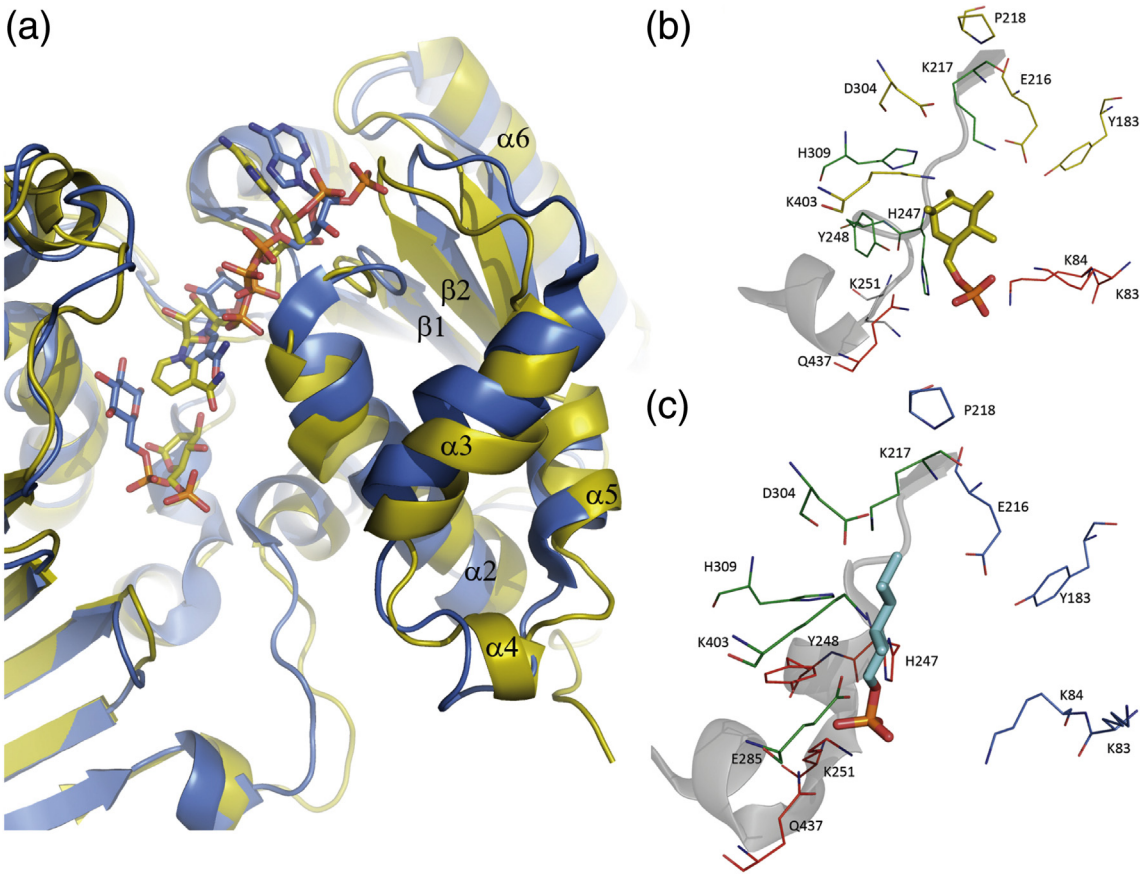

Fig. 9. Catalytic model of *Tc*G6PDH and conformational changes in elements and residues from the N-terminal domain involved in ligand binding. (a) Superimposition of the protein backbone corresponding to the catalytic (yellow cartoon) [18] and crystallographic (blue cartoon; chain A, PDB 5AQ1) [28] models of *Tc*G6PDH with bound ligands (G6P and $NADP^+$ for the catalytic model, and G6P and NADPH for the crystal structure). The secondary structure elements displaying shifts in their conformation are labeled (i.e., α2, 3, 4, 5 and 6, and β1 and 2). G6P and $NADP^+$(H) are shown as sticks with carbon atoms colored according to the backbone color selected for each structure. Residues that are important for G6P-binding (green lines, interacting with the sugar moiety; red lines, interacting with the phosphate groups) and for shaping the catalytic site (yellow or blue, for the corresponding structures) are shown for (b) the molecular dynamics model of the ternary enzyme-substrates complex and (c) the crystal structure of the enzyme–G6P–NADPH complex (chain A, PDB 5AQ1). For both models, the segment connecting β6 with α9 is shown as a cartoon (dark gray).

P218V mutant). Contiguous to P218 is K217, whose side chain interacts with either G6P O1 and O2 or the carboxylate of D304 (Fig. 9c), according to the crystallographic data. In the catalytic model, the side chain of K217 is almost aligned between the moieties of G6P and $NADP^+$, engaged in the chemical reaction and poised to interact with the sugar. Furthermore, the simulation shows a hydrogen bonding network between the side chains of E216 and Y183 that extends to K217, probably facilitating proton dissociation from the basic residue (Fig. 9b). In fact, mutation of K217 to isoleucine (K217I) impaired catalysis (~10-fold decrease in k_{cat}) and, to a minor degree, the apparent K_m for G6P (3-fold increase) when compared to the wild-type enzyme (Table 2). Further confirming that hydrophobic residues close to the active site favor anchoring of the nicotinamide ring (e.g., L80) [19], the P218V and K217I mutants showed increased affinity for $NADP^+$ (1.8-fold). At variance with H309, which is the catalytic base, K217 and P218 are not directly involved in the chemical steps of the reaction. In this regard, our kinetic and structural analysis suggests that they contribute to substrate-binding and orientation in the transition state.

Overall, and in line with the reaction mechanism obeyed by G6PDH (bi–bi ordered) [20,22,37], our comparative analysis suggests that the acquisition of a catalytically competent conformation in *Tc*G6PDH is likely induced by an ordered binding of substrates. Furthermore, it highlights that the N-terminal region of the Rossmann-fold domain of *Tc*G6PDH may have an

important conformational flexibility, amenable to stabilization by forming specific disulfide bonds.

Conclusions

The biological role of G6PDH in parasite´ redox homeostasis and drug resistance mechanisms [8,14,16,17] makes this enzyme an attractive target for anti-trypanosomatid drug development. Several three-dimensional structures of *Tc*G6PDH [19,23,29] led us now to a thorough comparison with its human counterpart, pinpointing pathogen-specific features.

The activity of human [41,42], cyanobacteria [43] and plant [44] G6PDH has been shown to benefit from an oligomeric (dimeric > tetrameric) assembly. However, at variance with the *T. cruzi* enzyme, oligomerization of these proteins depends on ligands (substrate, metabolites) and different physicochemical factors. Here we disclosed that *Tc*G6PDH forms highly stable tetramers with a single residue, R323, being responsible for stabilizing this oligomeric conformation. Importantly, conversion of *Tc*G6PDH into a predominantly dimeric form, proved detrimental for its enzyme activity. Our data suggest that the dimer–dimer contacts established via the R323 salt bridges are also important to stabilize the R323-containing loop and hence, the portion immediately N-terminal to it (i.e., the segment E285-T318), which includes amino acids engaged in G6P-binding and in catalysis. As shown here for the phylogenetically-related crithidial enzyme, a tetrameric conformation of G6PDH appears to be a common trait of kinetoplastid G6PDHs, even for those lacking R323. In the latter, a downstream and conserved arginine (R331 in *Cf*G6PDH) appears to surrogate the stabilizing role of R323 by forming an inter-subunit salt bridge with a nearby aspartate (D334) from a neighboring dimer. In contrast, G6PDHs from other Phyla lack basic residues in the equivalent positions altogether. A lineage-specific evolution of kinetoplastid G6PDHs has apparently favored the acquisition of a stable tetrameric assembly.

The activity of the plastidic isoforms of G6PDHs from plants and cyanobacteria is known to be subject of redox control, responding to reducing power requirements during the Calvin cycle for carbon fixation [45]. However, the cysteine residues responsible for such a regulation are not conserved among those organisms [46,47], nor with *Tc*G6PDH, making unlikely the hypothesis of a plastidic origin of the trypanosomal protein, as has been proposed for several other important metabolic enzymes [48]. Within the parasite-exclusive N-terminal extension of *Tc*G6PDH, and out of the several Cys residues exposed to the solvent, we have now found that C8 and C34 are the ones responsible for the formation of an intermolecular disulfide bridge between subunits of the dimer. These two cysteines proved to be key in mediating redox regulation of *Tc*G6PDH activity, as the kinetic parameters of the single or double Cys mutants were impaired with respect to the wild-type enzyme. The precise molecular events underlying the redox-dependent regulation of *Tc*G6PDH$_L$ activity are yet to be discovered. However, our structural and enzyme kinetic data lead us to posit that the reduction of the disulfide bridges from two subunits of the dimer likely distorts the conformation of the mobile N-terminal extension of *Tc*G6PDH$_L$. In turn, this would readily translate into conformational rearrangements and/or dynamic modulation of the juxtaposed structural elements, which are directly involved in ligand binding and/or in effecting the accessibility of the substrates to their binding sites. Additional structural stabilization within each protein subunit appears to be provided by a second set of cysteines (C53, C94 and C135) strictly conserved in G6PDHs from kinetoplastids. The crystal structures of truncated versions of *Tc*G6PDH showed that these three cysteines form intramolecular disulfide bridges (C53–C135 or C94–C135) and the corresponding cysteine point-mutants of the full-length protein proved detrimental for enzyme activity. This suggests a complex inter- and intramolecular redox regulation/stabilization of the G6PDH activity that shall be further analyzed in future studies.

The stable tetrameric and redox-regulated conformation of G6PDH that evolved in trypanosomes raises the question about the evolutionary constraints that might have led to divergence with the counterpart from other organisms. Probably, the more challenging growth conditions faced by these unicellular pathogens during their life cycle, acted as a selective pressure for developing a highly stable tetrameric conformation of G6PDH to ensure a steady supply of NADPH and/or ribose-5-phosphate. This evolutionary trait clearly differs from that evolved by G6PDH from several human lineages. Human G6PDH deficiency, commonly known as favism, is the most frequent enzymopathy associated with unstable enzyme conformations [49]. Several pieces of genetic and clinical evidences support that malaria infection acted as a major selective agent for the development of G6PDH deficiency as this renders erythrocytes unsuited for hosting *Plasmodium* sp. [50–53]. Altogether, this highlights the central role of G6PDH in cell metabolism and its propensity to undergo subtle structural changes with functional consequences. This is in line with the “new view” of protein structure–function evolution [54].

Human and *T. cruzi* G6PDHs share similar backbone structures, but the detailed molecular features presented in this work, as well as in prior studies from our laboratory [19] provide insights into the several regulatory and structural elements to be

selectively targeted as a rational strategy for anti-trypanosome drug development.

Experimental Procedures

Reagents

Molecular biology reagents were purchased from Fermentas (Thermo-Fisher Scientific), New England Biolab, Stratagene and Invitrogen. Chemical reagents were of analytical or higher grade and obtained from Sigma-Aldrich or AppliChem. Antibiotics were purchased from Invitrogen and Sigma-Aldrich. Oligonucleotides were synthesized by IDT. The kits for DNA purification were from Sigma-Aldrich and Invitrogen. All protein purification resins and columns were from General Electric Healthcare Life-Sciences (GE).

Plasmids

The constructs for the expression of N-terminally His-tagged full-length (*Tc*G6PDH$_L$; accession no. ABD72517.1) and truncated mutant lacking the first 37 amino acids (Δ37N-*Tc*G6PDH) of *T. cruzi* G6PDH were kindly provided by Dr. J. J. Cazzulo (Universidad Nacional de San Martín-CONICET, Argentina) [14]. The plasmid encoding for N-terminally His-tagged human G6PDH (*Hs*G6PDH, NCBI Nucleotide Reference Sequence NM_000402.3) was provided by Dr. Nial Hamilton (formerly at Manchester University, UK). The sequence encoding for *C. fasciculata* G6PDH (*Cf*G6PDH; accession no. CFAC1_290028300.1, http://tritrypdb.org/tritrypdb/) was *de novo* synthesized and inserted into pET28a(+) plasmid (Genscript), in frame with a vector sequence that adds an N-terminal 6x His-tag to the recombinant product.

The single C8S, C34S, K217I, P218V, H309G, R323G and C552S mutants were generated by using the Quick Change site-directed mutagenesis kit (Stratagene, La Jolla, CA, USA) and the construct pET28a(+)-*Tc*G6PDH$_L$ as template with the primer pairs indicated in supplementary Table 1. The PCR was performed in a total reaction volume of 50 µL according to the instructions of the supplier. One Shot® MAX Efficiency® DH5α™-T1R cells were transformed with the mutagenesis reaction. The double mutants C8S/C34S and R323G/C528R were generated using as template the construct pET28a(+)-*Tc*G6PDH$_L$ harboring the C8S and the R323G mutation, respectively, and the primer pairs Cys^{34}Ser Fwd/Cys^{34}Ser Rev. and Cys^{528}Arg Fwd/Cys^{528}Arg Rev. (Supplementary Table 1), respectively, and the Quick Change site-directed mutagenesis kit as indicated above.

The correctness of the targeted mutations was confirmed in at least three independent plasmids from each construct by DNA sequencing of the complementary chains (Molecular Biology Unit, Institut Pasteur de Montevideo, Uruguay or Macrogen, Korea).

Expression and purification of recombinant proteins

Escherichia coli Tuner (DE3) cells were transformed with the expression plasmids encoding for wild-type G6PDH from different organisms or the corresponding mutant versions. An overnight culture of transformed bacteria in LB medium with 50 µg/L kanamycin was inoculated at a ratio 1:100 in ZYM-5052 auto-induction medium to which 50 µg/L kanamycin was added, and cell growth was extended for 48 h at 25 °C and 200 rpm. Cells were harvested by centrifugation (5000*g*, 10 min, 4 °C) and suspended in 50 mM Tris (pH 8.0), 500 mM NaCl, 5 mM $MgCl_2$ (buffer A) plus 1 mM PMSF, 40 µg/mL TLCK, 150 nM pepstatin, 4 nM cystatin, or Complete™ Protease Inhibitor Cocktail (Sigma-Aldrich). Hen egg-white lysozyme was added (final concentration 1 mg/mL) and incubated for 60 min at 8 C°. After disruption by three cycles of sonication (30 pulses per minute at 45%–70% amplitude) using a macrotip in a Digital Sonifier 450 (Branson), the cell lysate was centrifuged at 15,000*g* (15 min, 4 °C), and the supernatant was further cleared of debris by centrifugation at 20,000*g* (30 min, 4 °C) and filtration through a 0.45-µm filter (Millipore). The cleared lysate was loaded onto a HisTrap column (GE) pre-equilibrated with buffer A. The column was washed with 10- and 5-column volume of buffer A and 5 mM imidazole in buffer A, respectively, and the protein was eluted with 500 mM imidazole in buffer A. The fractions containing the recombinant protein were collected, concentrated via ultrafiltration (10-kDa filter cutoff) and run on a Superdex 200 10/300 GL column (GE) pre-equilibrated with buffer A. Fractions containing the protein of interest, as assessed by Coomassie blue-stained SDS-PAGE (10% polyacrylamide), were collected, tested for enzyme-specific activity (see below), concentrated to 0.5 mg/mL and stored at 4 °C. Protein concentration was determined by the bicinchoninic acid assay or absorbance at 280 nm considering the molar extinction coefficient as calculated from the protein sequence.

Analytical SEC

The oligomeric state of the different recombinant proteins characterized in this work was studied by analytical gel-filtration chromatography on a Superdex 200 10/300 GL column (GE) coupled to an AKTA FPLC system (both from GE-Health Care) with online UV–visible detection. All chromatography experiments were performed at room temperature (RT) in 50 mM Tris–HCl (pH 7.5), 0.5 M NaCl and 5 mM $MgCl_2$ (reaction buffer) at a constant flow of 0.5 mL/min. The column was calibrated under identical running

conditions with molecular weight standards (ovalbumin, conalbumin, aldolase, ferritin and tyroglobulin, ranging 43–669 kDa). To test the effect of different ligands on protein oligomerization, *Tc*G6PDH$_L$ (50–150 μg/mL) was incubated for 30 min at 4 °C in reaction buffer consisting of 5 mM NADP$^+$, 5 mM G6P or 100 μM DHEA, and then resolved by gel filtration in reaction buffer containing the corresponding additives at identical concentrations. Similar amounts of protein were also subjected to gel filtration under different physicochemical conditions that involved the presence of a reducing agent (5 mM DTT) and high ionic strength (1 M NaCl). The effect of pH on *T. cruzi* and *C. fasciculata* G6PDHs' oligomeric structures was studied using 50 mM MES at pH 5.5 or 6.5 with 0.5 M NaCl and 5 mM $MgCl_2$. Protein elution was monitored online by 280-nm absorbance. The peaks of interest were subjected to enzymatic tests (see below) and denaturing 10% polyacrylamide gel electrophoresis under reducing [5% (v/v) ß-mercaptoethanol] and non-reducing conditions.

Structure determination

The crystallization conditions and X-ray diffraction data collection for recombinant Δ37N-*Tc*G6PDH in its apo-form and bound to G6P were previously described in Ref. [23]. Initial phases for the apo-form model were obtained by molecular replacement with PHASER [55] using the main chain atoms of 1QKI chain A (*Hs*G6PDH NADP$^+$-complex) [30] as search probe. The resulting model was used in initial rigid body refinement against data from *T. cruzi* G6P-G6PDH co-crystal using REFMAC5 [56]. Cycles of reciprocal space refinement were performed with REFMAC5 and later with Buster [57] using local non-crystallographic symmetry restraints and alternate TLS refinement. Sigma-weighted ($2mF_o - DF_c$ and $mF_o - DF_c$) electron density maps were used in Coot [58] to guide manual protein rebuilding and addition of solvent and ligand molecules. Validation was performed with Coot during model rebuilding and finally with MolProbity [59].

*Cf*G6PDH structure was generated by structure homology-modeling using the SWISS-MODEL server [60] and PDB 6D24 as template.

Protein and kinetics assays

Protein concentration was determined by the BCA method (Bicinchoninic Acid Protein Assay Kit, Sigma) using bovine serum albumin as standard. G6PDH activity was determined at ~ 25 °C by monitoring NADPH [(ε_{340} (NADPH) = 6220 M^{-1} cm^{-1}] formation at 340 nm. All reactions were performed in 50 mM Tris–HCl (pH 7.5) and 5 mM $MgCl_2$ in 150-μL final volume and started by the addition of G6P. For standard assays, NADP$^+$ and G6P were used at fixed concentrations of 500 μM and 6 mM, respectively, and with variable protein concentrations (10–897 nM). For determination of the apparent Michaelis constants (K_m^{app}) and maximum apparent velocities (V_{max}^{app}), each substrate was tested at five different concentrations (15 to 6000 μM for G6P and 1 to 800 μM for NADP$^+$) under fixed and saturating concentration of the second substrate involved (1 to 15 mM for G6P and 500 μM for NADP$^+$) using protein concentrations of 15 nM (*Tc*G6PDH$_L$), 16 nM (Δ37N-*Tc*G6PDH), 120 nM (C8S-*Tc*G6PDH$_L$), 340 nM (C34S-TcG6PDH$_L$), 330-390 nM (C8S/C34S-TcG6PDH$_L$), 160 nM (H309G-*Tc*G6PDH$_L$), 150 nM (K217I-*Tc*G6PDH$_L$), 138 nM (P218V-*Tc*G6PDH$_L$), 613 nM (R323G-*Tc*G6PDH$_L$), 897 nM (R323G/C528R-*Tc*G6PDH$_L$), 780 nM (C53S-*Tc*G6PDH$_L$), 549 nM (C94S-*Tc*G6PDH$_L$), 212 nM (C135S-*Tc*G6PDH$_L$) and 339 nM (C528R-*Tc*G6PDH$_L$). For determination of kinetic parameters under reducing conditions, the enzymatic assays were performed in the presence of 5 mM DTT. All measurements were performed at least in triplicate using a Cary 50 Bio spectrophotometer (Agilent Technologies, Santa Clara, CA, USA) at RT. The initial rates were determined with the Origin Pro 8.0 software (OriginLab Corporation, Northampton, MA, USA), and the apparent kinetic constants were calculated by nonlinear regression with the equation below using the GraphPad Prism 5.0 software (GraphPad Inc., San Diego, CA, USA).

$$v = V_{max}^{app} \frac{[S]}{K_M^{app} + [S]}$$

where V_{max}^{app} is the apparent maximum reaction rate, [S] is the initial concentration of either NADP$^+$ or G6P, and K_m^{app} is the apparent Michaelis constant. This approach is widely used for the analysis of the kinetics of G6P dehydrogenases [14].

Western blots

Anti-*Tc*G6PDH$_L$ serum was produced in mice (strain Balbc/J) using a standard immunization protocol with purified recombinant *Tc*G6PDH$_L$ as antigen, approved by the Institut Pasteur de Montevideo Committee on Animal Use and Ethics (CEUA Protocol No. 005-14). Mice were obtained from the in-house *specific pathogen-free* animal facility (Transgenic and Experimental Animal Unit, Institut Pasteur de Montevideo). The *Tc*G6PDH$_L$ cysteine mutants C8S, C34S and C8S/C34S were expressed and purified as described above and stored for 1 week at 4 °C in reaction buffer lacking any reducing agent. The different mutants at 2.5 μM were incubated 30 min in buffer A with 150 μM DTT, and the reducing agent was then removed using a NAP-5 desalting column (GE-Healthcare) pre-equilibrated in buffer A. A fraction of the DTT-reduced samples was stored on ice for SDS-PAGE analysis, and the remaining fraction was oxidized at 4 °C with

150 μM GSSG for 90 min. Each protein (300 ng) issued from non-reduced, DTT reduced and GSSG-oxidized samples was separated by SDS-PAGE (10% polyacrylamide) under non-reducing conditions and transferred to a polyvinylidene fluoride membrane (GE Healthcare). The membrane was blocked overnight at 4 °C in PBS + 0.2% (v/v) Tween-20 (PBS-T) and 5% (w/*v*) non-fat dry milk, washed with PBS-T and incubated with polyclonal mouse anti-*Tc*G6PDH$_L$ serum diluted 1:1000 in PBS-T at RT for 2 h. After three washing steps with PBS-T for 5 min each, the membrane was incubated for 1 h at RT with horseradish peroxidase-conjugated goat anti-mouse IgG (Amersham Biosciences, Buckinghamshire, England) diluted 1:10,000 in PBS-T. The membrane was extensively washed in PBS-T prior to chemoluminiscent detection of reactive bands with the Amersham ECL™ Western Blotting Detection Reagents (GE Healthcare) according to the manufacturer's instructions. Films (Amersham hyperfilm ECL, GE Healthcare) were exposed to the membranes during different times (1, 5 and 10 min) and developed for 1 min in developing solution (Sigma).

Accesion numbers

Structural coordinates of free *T. cruzi* G6PDH and in complex with G6P, have been deposited in the Protein Data Bank with IDs: 6D23 and 6D24, respectively.

Supplementary data to this article can be found online at https://doi.org/10.1016/j.jmb.2019.03.023.

CRediT authorship contribution statement

Cecilia Ortíz: Investigation, Formal analysis, Methodology, Writing - original draft. **Horacio Botti:** Formal analysis, Validation, Writing - original draft. **Alejandro Buschiazzo:** Data curation, Formal analysis, Validation, Supervision, Resources, Writing - original draft, Writing - review & editing. **Marcelo A. Comini:** Conceptualization, Formal analysis, Funding acquisition, Supervision, Validation, Visualization, Writing - original draft, Writing - review & editing.

Acknowledgments

This work was supported by a grant from the Agencia Nacional de Investigación e Innovación (ANII; Innova Uruguay, Agreement No. DCI-ALA/2007/19.040 between Uruguay and the European Commission) to M.A.C. C.O. and M.A.C. acknowledge the financial support from ANII (POS_NAC_2012_1_8803 and Comisión Académica de Posgrados, Universidad de la República, Uruguay) and PEDECIBA. Andrea Medeiros (Lab. Redox Biology of Trypanosomes) and Gabriel Fernández (Transgenic and Animal Experimentation Unit, Institut Pasteur de Montevideo) are gratefully acknowledged for technical assistance during production of *Tc*G6PDH antiserum, and Nicole Larrieux (Protein Crystallography Facility, Institut Pasteur de Montevideo) for assistance with crystallization and X-ray diffraction data collection.

Received 26 June 2018;
Received in revised form 4 March 2019;
Accepted 24 March 2019
Available online 28 March 2019
Keywords:
NADP;
pentose phosphate;
virulence;
disulfide bridge;
allosteric

Abbreviations used:
DTT, dithiotreitol; G6P, glucose 6-phosphate; G6PDH, glucose 6-phosphate dehydrogenase; *Hs*G6PDH, *Homo sapiens* glucose 6-phosphate dehydrogenase; Δ37N, deletion mutant lacking the first 37 N-terminal residues; Δ57N, deletion mutant lacking the first 57 N-terminal residues; PPP, pentose phosphate pathway; SDS-PAGE, sodium dodecyl sulfate–polyacrylamide gel electrophoresis; SEC, size exclusion chromatography; *T. cruzi*, *Trypanosoma cruzi*; *Tc*, *Trypanosoma cruzi*.

References

[1] R.L. Krauth-Siegel, M.A. Comini, Redox control in trypanosomatids, parasitic protozoa with trypanothione-based thiol metabolism, Biochim. Biophys. Acta 1780 (11) (2008) 1236–1248.
[2] F. Irigoín, L. Cibils, M.A. Comini, S.R. Wilkinson, L. Flohé, R. Radi, Insights into the redox biology of *Trypanosoma cruzi*: trypanothione metabolism and oxidant detoxification, Free Radic. Biol. Med. 45 (6) (2008) 733–742.
[3] P. Barderi, O. Campetella, A.C. Frasch, J.A. Santomé, U. Hellman, U. Pettersson, J.J. Cazzulo, The NADP+-linked glutamate dehydrogenase from *Trypanosoma cruzi*: sequence, genomic organization and expression, Biochem. J. 330 (2) (1998) 951–958.
[4] D.A. Maugeri, J.J. Cazzulo, The pentose phosphate pathway in *Trypanosoma cruzi*, FEMS Microbiol. Lett. 234 (1) (2004) 117–123 1.
[5] M.I. Esteve, J.J. Cazzulo, The 6-phosphogluconate dehydrogenase from *Trypanosoma cruzi*: the absence of two inter-subunit salt bridges as a reason for enzyme instability, Mol. Biochem. Parasitol. 133 (2) (2004) 197–207.
[6] A.E. Leroux, D.A. Maugeri, J.J. Cazzulo, C. Nowicki, Functional characterization of NADP-dependent isocitrate dehydrogenase isozymes from *Trypanosoma cruzi*, Mol. Biochem. Parasitol. 177 (1) (2011) 61–64.
[7] A.E. Leroux, D.A. Maugeri, F.R. Opperdoes, J.J. Cazzulo, C. Nowicki, Comparative studies on the biochemical properties

of the malic enzymes from *Trypanosoma cruzi* and *Trypanosoma brucei*, FEMS Microbiol. Lett. 314 (1) (2011) 25–33.
[8] S. Gupta, A.T. Cordeiro, P.A. Michels, Glucose-6-phosphate dehydrogenase is the target for the trypanocidal action of human steroids, Mol. Biochem. Parasitol. 176 (2) (2011) 112–115.
[9] S.K. Spaans, R.A. Weusthuis, J. van der Oost, S.W. Kengen, NADPH-generating systems in bacteria and archaea, Front. Microbiol. 6 (2015) 742.
[10] M.A. Comini, C. Ortíz, J.J. Cazzulo, Drug targets in trypanosomal and leishmanial pentose phosphate pathway, in: T. Jäger, O. Koch, L. Flohé (Eds.), Trypanosomatid Diseases [Internet], Wiley-VCH Verlag GmbH & Co. KGaA 2013, pp. 297–313.
[11] J. Kovářová, M.P. Barrett, The pentose phosphate pathway in parasitic trypanosomatids, Trends Parasitol. 32 (8) (2016) 622–634.
[12] R. Mancilla, C. Naquira, Comparative metabolism of C14-glucose in two strains of *Trypanosoma cruzi*, J. Protozool. 11 (1964) 509–513.
[13] J.K. Finzi, C.W. Chiavegatto, K.F. Corat, J.A. Lopez, O.G. Cabrera, A.A. Mielniczki-Pereira, W. Colli, M.J. Alves, F.R. Gadelha, *Trypanosoma cruzi* response to the oxidative stress generated by hydrogen peroxide, Mol. Biochem. Parasitol. 133 (1) (2004) 37–43.
[14] M. Igoillo-Esteve, J.J. Cazzulo, The glucose-6-phosphate dehydrogenase from *Trypanosoma cruzi*: its role in the defense of the parasite against oxidative stress, Mol. Biochem. Parasitol. 149 (2) (2006) 170–181.
[15] A.A. Mielniczki-Pereira, C.M. Chiavegatto, J.A. López, W. Colli, M.J. Alves, F.R. Gadelha, *Trypanosoma cruzi* strains, Tulahuen 2 and Y, besides the difference in resistance to oxidative stress, display differential glucose-6-phosphate and 6-phosphogluconate dehydrogenases activities, Acta Trop. 101 (1) (2007) 54–60.
[16] A.K. Ghosh, A.H. Sardar, A. Mandal, S. Saini, K. Abhishek, A. Kumar, B. Purkait, R. Singh, S. Das, R. Mukhopadhyay, S. Roy, P. Das, Metabolic reconfiguration of the central glucose metabolism: a crucial strategy of *Leishmania donovani* for its survival during oxidative stress, FASEB J. 29 (5) (2015) 2081–2098.
[17] A.K. Ghosh, S. Saini, S. Das, A. Mandal, A.H. Sardar, M.Y. Ansari, K. Abhishek, A. Kumar, R. Singh, S. Verma, A. Equbal, V. Ali, P. Das, Glucose-6-phosphate dehydrogenase and trypanothione reductase interaction protects *Leishmania donovani* from metalloid mediated oxidative stress, Free Radic. Biol. Med. 106 (2017) 10–23.
[18] G.F. Mercaldi, A.T. Ranzani, A.T. Cordeiro, Discovery of new uncompetitive inhibitors of glucose-6-phosphate dehydrogenase, J. Biomol. Screen. 19 (10) (2014) 1362–1371.
[19] C. Ortiz, F. Moraca, A. Medeiros, M. Botta, N. Hamilton, M.A. Comini, Binding mode and selectivity of steroids towards glucose-6-phosphate dehydrogenase from the pathogen *Trypanosoma cruzi*, Molecules. 21 (3) (2016) 368.
[20] S. Funayama, S. Funayama, I.Y. Ito, L.A. Veiga, *Trypanosoma cruzi*: kinetic properties of glucose-6-phosphate dehydrogenase, Exp. Parasitol. 43 (2) (1977) 376–381.
[21] N. Heise, F.R. Opperdoes, Purification, localization and characterization of glucose-6-phosphate dehydrogenase of *Trypanosoma brucei*, Mol. Biochem. Parasitol. 99 (1999) 21–32.
[22] A.T. Cordeiro, O.H. Thiemann, P.A. Michels, Inhibition of *Trypanosoma brucei* glucose-6-phosphate dehydrogenase by human steroids and their effects on the viability of cultured parasites, Bioorg. Med. Chem. 17 (6) (2009) 2483–2489.
[23] C. Ortíz, N. Larrieux, A. Medeiros, H. Botti, M. Comini, A. Buschiazzo, Expression, crystallization and preliminaryX-ray crystallographic analysis of glucose-6-phosphate dehydrogenase from the humanpathogen *Trypanosoma cruzi* in complex with substrate, Acta Crystallogr. Sect. F 67 (2011) 1457–1461.
[24] D.S. Shreve, H.R. Levy, On the molecular weight of human glucose 6-phosphate dehydrogenase, Biochem. Biophys. Res. Commun. 78 (1977) 1369–1375.
[25] F. Schaeffer, R.Y. Stanier, Glucose-6- phosphate dehydrogenase of anabaena sp. kinetics and molecular properties, Arch. Microbiol. 116 (1978) 9–19.
[26] P. Rowland, A.K. Basak, S. Gover, H.R. Levy, M.J. Adams, The three-dimensional structure of glucose 6-phosphate dehydrogenase from *Leuconostoc mesenteroides* refined at 2.0 Å resolution, Structure 2 (11) (1994) 1073–1087.
[27] S. Sundaram, H. Karakaya, D.J. Scanlan, N.H. Mann, Multiple oligomeric forms of glucose-6-phosphate dehydrogenase in cyanobacteria and the role of OpcA in the assembly process, Microbiology 144 (Pt 6) (1998) 1549–1556.
[28] V. Comakli, E. Akkemik, M. Ciftci, O.I. Kufrevioglu, Purification and characterization of glucose 6-phosphate dehydrogenase enzyme from rainbow trout (*Oncorhynchus mykiss*) liver and investigation of the effects of some metal ions on enzyme activity, Toxicol. Ind. Health 31 (2015) 403–411.
[29] G.F. Mercaldi, A. Dawson, W.N. Hunter, A.T. Cordeiro, The structure of a *Trypanosoma cruzi* glucose-6-phosphate dehydrogenase reveals differences from the mammalian enzyme, FEBS Lett. 590 (16) (2016) 2776–2786.
[30] S.W. Au, S. Gover, V.M. Lam, M.J. Adams, Human glucose-6-phosphate dehydrogenase: the crystal structure reveals a structural NADP(+) molecule and provides insights into enzyme deficiency, Structure 8 (3) (2000) 293–303.
[31] P. Cohen, M.A. Rosemeyer, Glucose-6-phosphate dehydrogenase from human erythrocytes, Methods Enzymol. 41 (1975) 208–214.
[32] A. Bonsignore, R. Cancedda, I. Lorenzoni, M.E. Cosulich, A. De Flora, Human erythrocyte glucose 6-phosphate dehydrogenase. Physical properties, Biochem. Biophys. Res. Commun. 43 (1) (1971) 94–101.
[33] X.T. Wang, P.C. Engel, Clinical mutants of human glucose 6-phosphate dehydrogenase: impairment of NADP(+) binding affects both folding and stability, Biochim. Biophys. Acta 1792 (8) (2009) 804–809.
[34] X.T. Wang, T.F. Chan, V.M. Lam, P.C. Engel, What is the role of the second "structural" NADP+-binding site in human glucose 6-phosphate dehydrogenase? Protein Sci. 17 (8) (2008) 1403–1411.
[35] S. Filosa, V. Calabrò, D. Vallone, V. Poggi, P. Mason, D. Pagnini, F. Alfinito, B. Rotoli, G. Martini, L. Luzzatto, G. Battistuzzi, Molecular basis of chronic non-spherocytic haemolytic anaemia: a new G6PD variant (393 Arg–His) with abnormal KmG6P and marked in vivo instability, Br. J. Haematol. 80 (1) (1992) 111–116.
[36] M. Kotaka, S. Gover, L. Vandeputte-Rutten, S.W. Au, V.M. Lam, M.J. Adams, Structural studies of glucose-6-phosphate and NADP+ binding to human glucose-6-phosphate dehydrogenase, Acta Crystallogr. D Biol. Crystallogr. 61 (Pt 5) (2005) 495–504.
[37] M.S. Cosgrove, C. Naylor, S. Paludan, M.J. Adams, H.R. Levy, On the mechanism of the reaction catalyzed by glucose 6-phosphate dehydrogenase, Biochemistry 37 (9) (1998) 2759–2767.
[38] M.S. Cosgrove, S. Gover, C.E. Naylor, L. Vandeputte-Rutten, M.J. Adams, H.R. Levy, An examination of the role of asp-

177 in the His-Asp catalytic dyad of *Leuconostoc mesenteroides* glucose 6-phosphate dehydrogenase: X-ray structure and pH dependence of kinetic parameters of the D177N mutant enzyme, Biochemistry 39 (49) (2000) 15002–15011.
[39] C.E. Naylor, S. Gover, A.K. Basak, M.S. Cosgrove, H.R. Levy, M.J. Adams, NADP+ and NAD+ binding to the dual coenzyme specific enzyme *Leuconostoc mesenteroides* glucose 6-phosphate dehydrogenase: different interdomain hinge angles are seen in different binary and ternary complexes, Acta Crystallogr. D Biol. Crystallogr. 57 (Pt 5) (2001) 635–648.
[40] C.E. Naylor, S. Gover, A.K. Basak, M.S. Cosgrove, H.R. Levy, M.J. Adams, NADP+ and NAD+ binding to the dual coenzyme specific enzyme *Leuconostoc mesenteroides* glucose 6-phosphate dehydrogenase: different interdomain hinge angles are seen in different binary and ternary complexes, Acta Cryst D57 (2001) 635–648.
[41] P. Cohen, M.A. Rosemeyer, The molecular weight and subunit structure of glucose-6-phosphate dehydrogenase from human erythrocytes, FEBS Lett. 1 (3) (1968) 147–149.
[42] A.T. Ranzani, A.T. Cordeiro, Mutations in the tetramer interface of human glucose-6-phosphate dehydrogenase reveals kinetic differences between oligomeric states, FEBS Lett. 591 (9) (2017) 1278–1284.
[43] K.D. Hagen, J.C. Meeks, The unique cyanobacterial protein OpcA is an allosteric effector of glucose-6-phosphate dehydrogenase in Nostoc punctiforme ATCC 29133, J. Biol. Chem. 276 (15) (2001) 11477–11486.
[44] Z.Q. Hong, L. Copeland, Isoenzymes of glucose 6-phosphate dehydrogenase from the plant fraction of soybean nodules, Plant Physiol. 96 (3) (1991) 862–867.
[45] C. Oesterhelt, S. Klocke, S. Holtgrefe, V. Linke, A.P. Weber, R. Scheibe, Redox regulation of chloroplast enzymes in *Galdieria sulphuraria* in view of eukaryotic evolution, Plant Cell Physiol. 48 (9) (2007) 1359–1373.
[46] J. Udvardy, G. Borbely, A. Juhász, G.L. Farkas, Thioredoxins and the redox modulation of glucose-6-phosphate dehydrogenase in *Anabaena* sp. strain PCC 7120 vegetative cells and heterocysts, J. Bacteriol. 157 (2) (1984) 681–683.
[47] I. Wenderoth, R. Scheibe, A. von Schaewen, Identification of the cysteine residues involved in redox modification of plant plastidic glucose-6-phosphate dehydrogenase, J. Biol. Chem. 272 (43) (1997) 26985–26990.
[48] V. Hannaert, E. Saavedra, F. Duffieux, J.P. Szikora, D.J. Rigden, P.A. Michels, F.R. Opperdoes, Plant-like traits associated with metabolism of *Trypanosoma* parasites, Proc. Natl. Acad. Sci. U. S. A. 100 (3) (2003) 1067–1071.
[49] E. Beutler, G6PD deficiency, Blood 84 (1994) 3613–3636.
[50] A.C. Allison, D.F. Clyde, Malaria in African children with deficient erythrocyte glucose-6 phosphate dehydrogenase, Br. Med. J. 1 (1961) 1346–1349.
[51] E.F. Roth, C. Raventos-Suarez, A. Rinaldi, R.L. Nagel, Glucose-6-phosphate dehydrogenase deficiency inhibits in vitro growth of *Plasmodium falciparum*, Proc. Natl. Acad. Sci. U. S. A. 80 (1983) 298–299.
[52] C. Ruwende, S.C. Khoo, R.W. Snow, S.N. Yates, D. Kwiatkowski, S. Gupta, P. Warn, C.E. Allsopp, S.C. Gilbert, N. Peschu, Natural selection of hemi- and heterozygotes for G6PD deficiency in Africa by resistance to severe malaria, Nature 376 (1995) 246–249.
[53] S.A. Tishkoff, R. Varkonyi, N. Cahinhinan, S. Abbes, G. Argyropoulos, G. Destro-Bisol, A. Drousiotou, B. Dangerfield, G. Lefranc, J. Loiselet, A. Piro, M. Stoneking, A. Tagarelli, G. Tagarelli, E.H. Touma, S.M. Williams, A.G. Clark, Haplotype diversity and linkage disequilibrium at human G6PD: recent origin of alleles that confer malarial resistance, Science 293 (2001) 455–462.
[54] L.C. James, D.S. Tawfik, Conformational diversity and protein evolution—a 60-year-old hypothesis revisited, Trends Biochem. Sci. 28 (7) (2003) 361–368.
[55] A.J. McCoy, R.W. Grosse-Kunstleve, P.D. Adams, M.D. Winn, L.C. Storoni, R.J. Read, Phaser crystallographic software, J. Appl. Crystallogr. 40 (Pt 4) (2007) 658–674.
[56] G.N. Murshudov, P. Skubák, A.A. Lebedev, N.S. Pannu, R.A. Steiner, R.A. Nicholls, M.D. Winn, F. Long, A.A. Vagin, REFMAC5 for the refinement of macromolecular crystal structures, Acta Crystallogr. D Biol. Crystallogr. 67 (Pt 4) (2011) 355–367.
[57] O.S. Smart, T.O. Womack, C. Flensburg, P. Keller, W. Paciorek, A. Sharff, C. Vonrhein, G. Bricogne, Exploiting structure similarity in refinement: automated NCS and target-structure restraints in BUSTER, Acta Crystallogr. D Biol. Crystallogr. 68 (Pt 4) (2012) 368–380.
[58] P. Emsley, B. Lohkamp, W.G. Scott, K. Cowtan, Features and development of Coot, Acta Crystallogr. D Biol. Crystallogr. 66 (Pt 4) (2010) 486–501.
[59] V.B. Chen, W.B. Arendall III, J.J. Headd, D.A. Keedy, R.M. Immormino, G.J. Kapral, L.W. Murray, J.S. Richardson, D.C. Richardson, MolProbity: all-atom structure validation for macromolecular crystallography, Acta Crystallogr. D Biol. Crystallogr. 66 (Pt 1) (2010) 12–21.
[60] A. Waterhouse, M. Bertoni, S. Bienert, G. Studer, G. Tauriello, R. Gumienny, F.T. Heer, T.A.P. de Beer, C. Rempfer, L. Bordoli, R. Lepore, T. Schwede, SWISS-MODEL: homology modelling of protein structures and complexes, Nucleic Acids Res. 46 (W1) (2018) W296–W303.